



## RESEARCH ARTICLE

10.1029/2019JB017835

## Key Points:

- Teleseismic receiver functions beneath the Eastern Cordillera plateau of Colombia are consistent with the presence of major crustal thrusts and shear zones where shortening may have been accommodated
- A high seismic speed lower crustal layer beneath two Mio-Pliocene volcanic domes can be interpreted as magmatic underplating
- Mio-Pliocene volcanism in the Eastern Cordillera of Colombia may be related to slab flattening

## Supporting Information:

- Supporting Information S1

## Correspondence to:

G. Monsalve,  
gmonsalmvem@unal.edu.co

## Citation:

Monsalve, G., Jaramillo, J. S., Cardona, A., Schulte-Pelkum, V., Posada, G., Valencia, V., & Poveda, E. (2019). Deep crustal faults, shear zones, and magmatism in the Eastern Cordillera of Colombia: Growth of a plateau from teleseismic receiver function and geochemical Mio-Pliocene volcanism constraints. *Journal of Geophysical Research: Solid Earth*, 124, 9833–9851. <https://doi.org/10.1029/2019JB017835>

Received 10 APR 2019

Accepted 21 AUG 2019

Accepted article online 30 AUG 2019

Published online 10 SEP 2019

## Deep Crustal Faults, Shear Zones, and Magmatism in the Eastern Cordillera of Colombia: Growth of a Plateau From Teleseismic Receiver Function and Geochemical Mio-Pliocene Volcanism Constraints

G. Monsalve<sup>1</sup> , J. S. Jaramillo<sup>1</sup> , A. Cardona<sup>1</sup>, V. Schulte-Pelkum<sup>2</sup> , G. Posada<sup>1,3</sup> , V. Valencia<sup>4</sup> , and E. Poveda<sup>5</sup>

<sup>1</sup>Facultad de Minas, Universidad Nacional de Colombia, Medellín, Colombia, <sup>2</sup>Cooperative Institute for Research in Environmental Sciences (CIRES), University of Colorado Boulder, Boulder, CO, USA, <sup>3</sup>Sistema de Alerta Temprana de Medellín y el Valle de Aburrá (SIATA), Medellín, Colombia, <sup>4</sup>School of Earth and Environmental Science, Washington State University, Pullman, WA, USA, <sup>5</sup>Red Sismológica Nacional de Colombia (RSNC), Servicio Geológico Colombiano (SGC), Bogotá, Colombia

**Abstract** The Eastern Cordillera of Colombia, in the northern Andes, is an example of an orogen in which Mesozoic basins were compressed during the Cenozoic, forming a ~2,500-m-high plateau in its northern portion. Significant shortening and crustal thickening have contributed to the construction of the present topography and elevation. In this contribution, we combine the use of teleseismic receiver functions, Hf isotopes, whole-rock geochemistry, and U-Pb dating to help elucidate the main mechanisms that played a role in the crustal thickening and uplift of the cordillera. Receiver functions calculated for three stations on top of the plateau are consistent with the presence of thrusts that converge into major crustal interfaces at upper-middle crustal depths; they also suggest the existence of two crustal anisotropic layers beneath the western flank of the cordillera, which we interpret to have formed as a result of shearing. In the northern portion of the plateau, in the area where two Mio-Pliocene volcanic domes and their related deposits outcrop, a lower crustal high seismic velocity layer is suggested by the receiver functions; we propose magmatic underplating for the origin of this layer. The geochemical characteristics of the volcanic rocks in the area are consistent with partial melt in a mantle influenced by slab-related fluids; this magma could have been added to the crust and portions of it ascended and reached the surface, experiencing assimilation and differentiation during the process. We hypothesize that this Mio-Pliocene volcanism was related to flattening of the Nazca subducting slab.

### 1. Introduction

The Eastern Cordillera (EC) in the Colombian Andes (Figure 1) was uplifted during the Cenozoic by stacking up pieces of crust in a fold-and-thrust belt that involved the basement (Babault et al., 2013; Bayona et al., 2013; Corredor, 2003; Horton et al., 2010; Mora et al., 2008; Mora et al., 2013; Saylor et al., 2012; Tesón et al., 2013), forming a plateau in its northern portion, with an average elevation of ~2,500 m above sea level (Figure 2). Normal faults that were reactivated as reverse faults played a crucial role in the construction of the present EC (Bayona et al., 2013; Mora et al., 2013). Crustal thickness in the central portion of the EC may locally reach values as high as 60 km at ~4°N (Figure 2), and Moho depths between 46 and 53 km have been estimated for the eastern flank and the northern portion of the EC Plateau (Poveda et al., 2015). Thickening of the crust in this area can be mainly attributed to shortening (Mora-Paez et al., 2016; Poveda et al., 2015), but magmatic additions, commonly neglected, may have also played an additional role as there is evidence for relatively recent volcanic activity (late Miocene through early Pleistocene) in the area (Bernet et al., 2016; Pardo, Cepeda, et al., 2005; Renzoni, 1967; Vesga & Jaramillo, 2009); Figure 2 shows the location of the volcanic domes associated with this activity.

In this study, our purpose is to contribute to the knowledge of the geometry of major crustal features in the EC Plateau and discuss the different mechanisms that may have contributed to the evolution of the orogenic crust in this segment of the Northern Andes. First, we apply a technique outlined by Schulte-Pelkum and Mahan (2014a, 2014b), which uses teleseismic radial and transverse receiver functions to image major

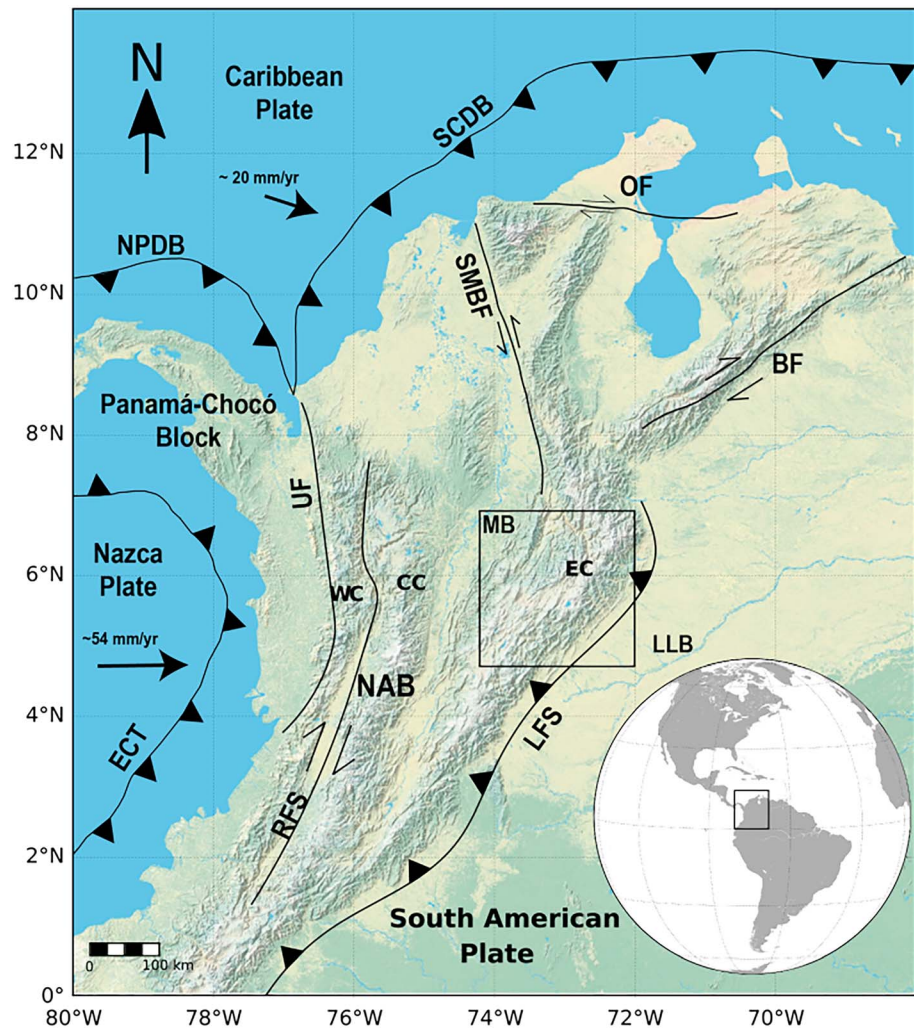


**Figure 1.** Simplified tectonic map of northwestern South America, showing the main tectonic and physiographic units. Black box encloses the study area, which is presented in detail in Figure 2. Plate motion vectors are relative to stable South America (Mora-Paez et al., 2019; Trenkamp et al., 2002). NAB = North Andes Block; EC = Eastern Cordillera; CC = Central Cordillera; WC = Western Cordillera; ECT = Ecuador-Colombia Trench; NPDB = North Panama Deforming Belt; SCDB = South Caribbean Deformed Belt; OF = Oca Fault; SMBF = Santa Marta-Bucaramanga Fault; BF = Boconó Bault; RFS = Romeral Fault Zone; LFS = Llanos Fault System; LLB = Llanos Basin; MB = Magdalena Basin; UF = Uramita Fault.

crustal interfaces, faults, and shear zones. This method allows the identification of the most prominent structures at a crustal scale and may give information about features at depths that are difficult to detect with conventional seismic methods. We also use new geochronological and geochemical results from the Mio-Pliocene volcanism exposed in the EC, ~160 km northeast of Bogota (Bernet et al., 2016; Pardo, Cepeda, et al., 2005; Pardo, Jaramillo, et al., 2005; Vesga & Jaramillo, 2009), to argue that both thrusting and magmatic additions have played a role in the present crustal configuration of the EC plateau.

## 2. Tectonic Setting of the EC and Geology of the Paipa-Iza Volcanic Complexes

The study region is located within the northernmost segment of the Andean chain, in the northwestern corner of South America, where three major tectonic plates and at least two tectonic blocks converge (Figure 1). The Colombian cordilleras are located in the so-called North Andean Block, which is currently experiencing intense deformation and is escaping to the NE as a result of its interaction with the Nazca, Caribbean and South American Plates, and the Panama-Chocó Block (Kellogg & Vega, 1995; Trenkamp et al., 2002). A

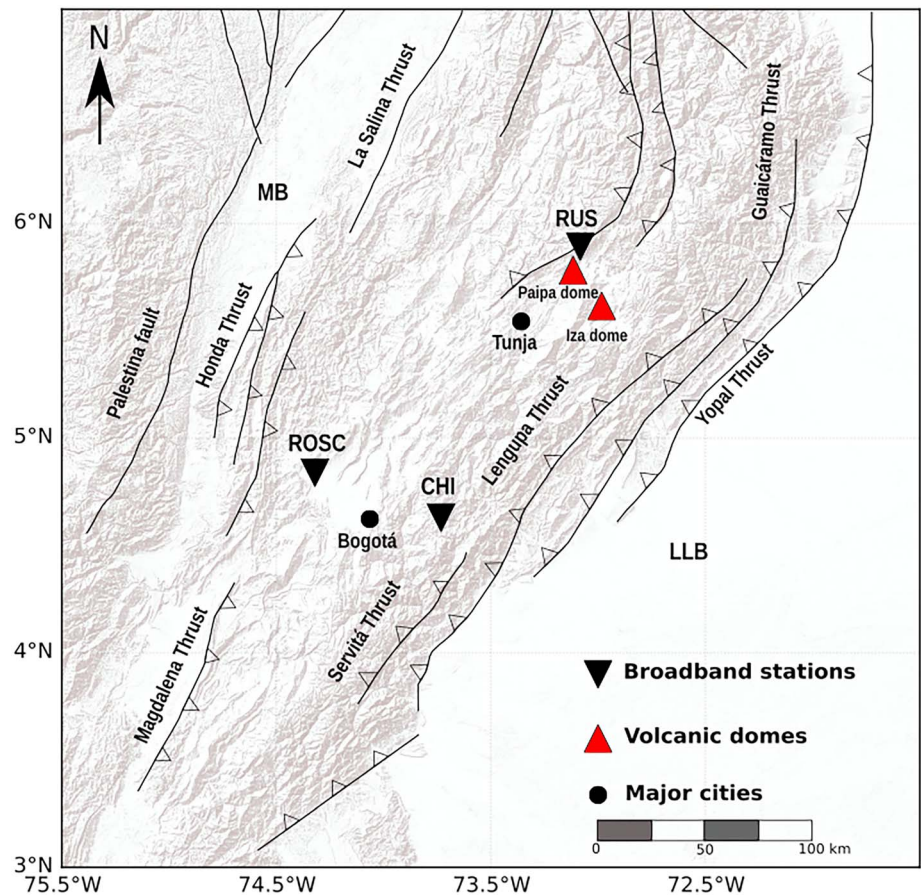


**Figure 2.** Detail of the study area in the central portion of the Eastern Cordillera, showing the main fault systems in the area, the broadband seismological stations (inverted black triangles, coded as CHI, ROSC, and RUS), and the main volcanic domes (red triangles at the localities of Paipa and Iza). Surrounding the Paipa and Iza domes, there are volcanic deposits and local thrust faults (Pardo, Cepeda, et al., 2005). MB = Magdalena Basin; LLB = Llanos Basin.

combination of different processes along the continental margin, including subduction, accretion, and collision, has built the cordilleran system of Colombia. The three main mountain ranges in the Colombian Andes are roughly delimited by major fault systems and sutures that define a complex configuration of exotic accreted terranes in the continental margin of northwestern South America (Cediel et al., 2003; Hincapié-Gómez et al., 2018; Restrepo & Toussaint, 1988).

The current EC is geographically located between the Magdalena and the Llanos Basins (Figures 1 and 2). It is composed of Precambrian and Paleozoic metamorphic basement covered by Mesozoic and Cenozoic sedimentary rocks (Irving, 1971). Its time of uplift is debated (Anderson et al., 2015; Gómez et al., 2003; Mora et al., 2008, 2010, 2014; Mora-Paez et al., 2016; Pérez-Angel & Molnar, 2017), but it is generally accepted that it was raised during the Cenozoic by inversion of Mesozoic extensional basins (Bayona et al., 2013; Mora et al., 2013). Previous normal faults reactivated as reverse, and the result is a bivergent fold and thrust system (Cortés et al., 2006; Mora et al., 2013; Taboada et al., 2000) that forms a plateau in its northern portion (Figure 2). Tectonic activity in the EC has been more or less continuous since middle Paleocene-Eocene through Holocene, with an important cooling stage after 10 Ma inferred from apatite and zircon fission track ages (Mora et al., 2010, 2015; Parra et al., 2009, 2012). Mora et al. (2008, 2010, 2015) and Parra et al. (2009) have proposed that most of the deformation has been concentrated in the eastern flank of the cordillera since Mio-Pliocene times.

Two relatively small circular regions characterized by the exposure of proximal pyroclastic sequences and domes of alkaline andesite and rhyolite composition have been documented in the EC near the towns of Paipa and Iza (Figure 2; Monsalve et al., 2011; Pardo, Cepeda, et al., 2005; Pardo, Jaramillo, et al., 2005;

Renzoni, 1967; Vesga & Jaramillo, 2009). This volcanism is located at least 560 km away from the current Nazca plate trench and within a latitudinal segment in which the modern arc front seems to be absent. Pardo, Cepeda, et al. (2005), Pardo, Jaramillo, et al. (2005) showed that the volcanic record near Paipa includes a series of intercalated block and ash flows, tuffs, accretionary lapilli, and pyroclastic pumice levels. Based on U-Pb zircon geochronology and Ar-Ar and K-Ar analyses, this volcanic record may extend from 5.9 to 1.8 Ma (Bernet et al., 2016; Pardo, Cepeda, et al., 2005). For the Iza volcanic record, Monsalve et al. (2011) considered the existence of two main domes and intrusive breccia with limited or almost absent surficial expression of the volcanic products. Temporal constraints for the Iza locality, based on zircon fission track thermochronology, have yielded ages between 5.4 and 0.9 Ma (Bernet et al., 2016).

This volcanic record is characterized by superimposed hydrothermal alteration, marked by the presence of clay and sulfurs (Moyano & Vallejo, 2015), as well as veins of chlorite and albite and the replacement of plagioclase by epidote (Alfaro et al., 2010). Evidence of an active geothermal system includes hot springs that can reach 74 °C (Alfaro et al., 2010; Moyano & Vallejo, 2015), and the presence of partial annealing in zircons has been also considered as potentially connected to high heat flow conditions in the two regions (Bernet et al., 2016). This volcanism cuts Upper Cretaceous gray and black shales, sandstones, and limestones included in the Une, Churuvita, and Conejo Formations (Renzoni, 1967) that are also found as xenoliths (Monsalve et al., 2011).

### 3. Data and Methods

#### 3.1. Teleseismic Receiver Functions

We used the data from three broadband stations of the National Seismological Network of Colombia (Figure 2), operated by the Colombian Geological Survey (SGC from the Spanish *Servicio Geológico Colombiano*): For Station CHI, located near the eastern flank of the EC plateau, we used the data from 2008 through 2015; for Station ROSC (western flank of the plateau), data from 2003 to 2015; and for Station RUS (near the northern end of the plateau), we included seismic data between 2008 and 2016. For each station, we used teleseismic events at epicentral distances between 29° and 90° and magnitudes greater than 5.5. P to S radial and transverse receiver functions were computed using an iterative time domain deconvolution technique (Ligorria & Ammon, 1999). More information about the receiver function calculation can be found in Poveda et al. (2015). Since we are interested in resolving intracrustal features, in this case the bandwidth factor (denoted by the Gaussian parameter “a” in the iterative deconvolution terminology) was 5.0, which corresponds to a low-pass filter with a relatively high corner frequency of 2.4 Hz.

Before azimuthal binning and stacking of the receiver functions, a move out correction was carried out given the variety of epicentral distances of the used events, so we equalized our seismic traces to a slowness value of 0.06 s/km. In order to detect intracrustal faults or shear zones, we follow the procedure described in Schulte-Pelkum and Mahan (2014a, 2014b). Figure 3 shows radial and tangential stacked receiver functions for Station CHI, using 10° bins with no overlapping. Subsequently, the azimuthally binned and then averaged radial receiver function was subtracted from individual traces (Figure 4a), tangential receiver functions were shifted 90° in back azimuth (Figure 4b), and the traces were then combined (radials plus tangentials; Figure 4c) to isolate the P-SH scattered signal. Using the combined traces, a degree-1 harmonic function was fitted to the receiver function amplitude at each time point, such that we picked those time points at which the amplitude of the fitted harmonic function is at its maximum. In Figure 5, it can be seen that there are two noticeable maxima at ~0 and 0.6 s.

To assess the plausibility of the hypotheses about crustal structures, we computed synthetics using the Raysum algorithm of Frederiksen and Bostock (2000) and conducted the same procedures as for the data (demeaning of the radial traces, rotation of the tangentials, and addition). Figure 6 shows the result of the combined azimuthally varying receiver functions from Figure 4c (Figure 6a) as well as the synthetics (Figure 6b), which were computed assuming a dipping isotropic interface at 7 km beneath the station, with an attitude 45/310 (dip/dip direction), a WNW dipping interface. In Figure 6a, vertical green lines indicate the times of maximum amplitude of the fitted harmonic functions; the horizontal green line shows the azimuth at which the waveform polarity switches, which should correspond to the strike of the dipping interface.

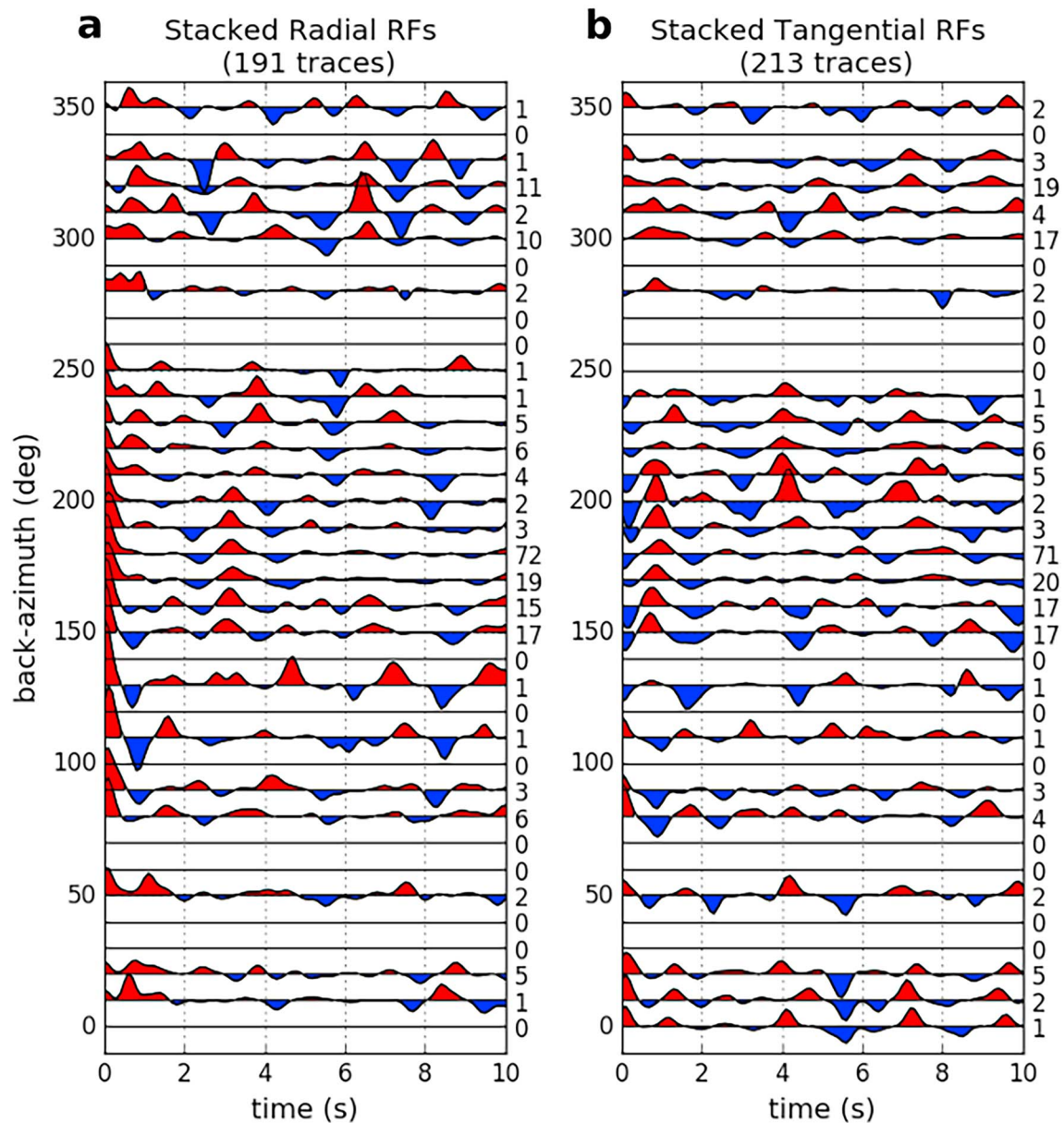


**Figure 3.** Stacked radial (a) and tangential (b) teleseismic RFs at Station CHI. The number of the stacked azimuthal receiver functions per bin is indicated on the right. Traces have been equalized to a slowness value of 0.06 s/km. No corrections have been applied on the amplitude. RF = receiver function.

### 3.2. U-Pb Dating, Hf Isotope Analysis, and Geochemistry

We collected and described several samples on the Iza and Paipa regions and selected a rhyolite for detailed analysis. For the U-Pb laser ablation-inductively coupled plasma mass spectrometry (ICP-MS) zircon geochronology, traditional techniques, including crushing, fragmentation, pulverization, and sieving, were carried out at Zirchron Lab. Wilfley table and Frantz isodynamic were used to concentrate heavy and nonmagnetic minerals, respectively. Methylene iodide, with a density of 3.30 to 3.33 g/cm<sup>3</sup>, was used to concentrate the zircon crystals, and subsequently, they were handpicked under the microscope and mounted in an epoxy puck; then the zircons were polished and exposed. These analyses were conducted at the Washington State University Geoanalytical Lab, using a New Wave Nd: YAG UV 213-nm laser coupled to a ThermoFinnigan Element 2 single collector, double-focusing, magnetic sector ICP-MS. Laser spot size and repetition rates were 30 microns and 10 Hz, respectively. He and Ar carrier gases delivered the

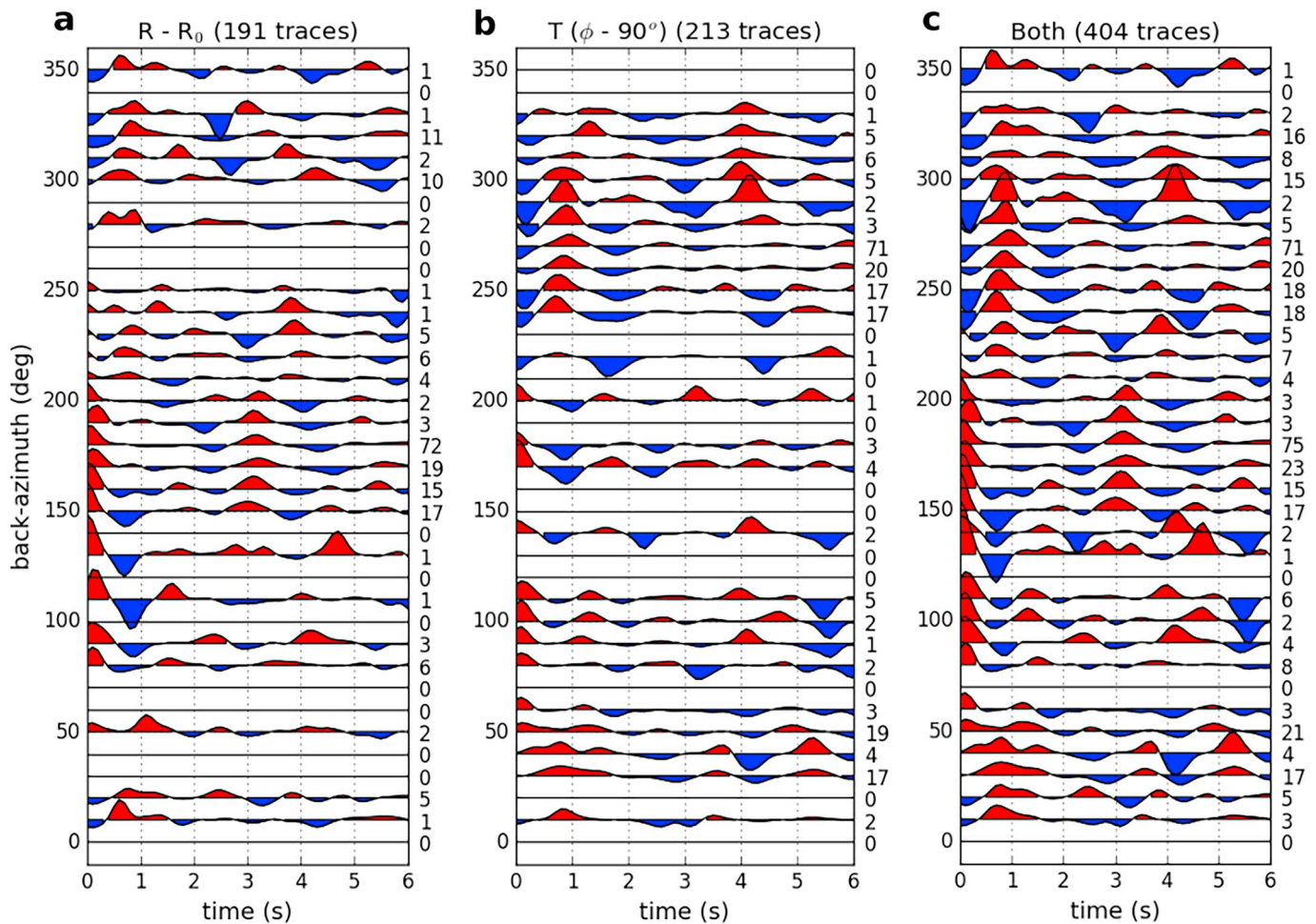


**Figure 4.** Processing of the receiver functions at Station CHI to highlight the azimuthal variations. (a) Azimuthal average of the radial receiver functions was subtracted from the radials. (b) Tangential receiver functions were shifted by  $90^\circ$  in backazimuth. (c) Demeaned radial and shifted tangentials were added (a + b) to generate a consolidated azimuthally varying set of receiver functions. The number of the stacked azimuthal receiver functions per bin is indicated on the right. Details of the method can be found in Schulte-Pelkum and Mahan (2014a, 2014b). Times were corrected to a slowness value of 0.06 s/km before stacking.

sample aerosol to the plasma. Each analysis consisted of a short blank analysis followed by 300 sweeps through masses 204, 206, 207, 208, 232, 235, and 238, taking approximately 35 s. The method, operating procedures, parameters, and fractional corrections are described by Chang et al. (2006). For this study, the Plešovice zircon, which is characterized by a  $^{206}\text{Pb}/^{238}\text{U}$  age of  $337.13 \pm 0.37$  Ma (Sláma et al., 2008), was used as a standard, and 91,500 zircon was used to monitor U and Th concentrations (Wiedenbeck et al., 1995). Common Pb corrections were made on these analyses using the  $^{207}\text{Pb}$  method (Williams, 1998). U-Pb data were reduced using Isoplot (Ludwig, 2012). Results are presented in supporting information Table S1.

The Hf isotope geochemistry in zircons was performed on a rhyolite dyke sample at the Geoanalytical Lab of the Washington State University, using a ThermoFinnigan Neptune<sup>TM</sup> MC-ICP-MS equipped with nine faraday collectors interfaced with a New Wave<sup>TM</sup> 213-nm UP Nd-YAG laser. The laser was operated at a pulse with a rate of 10 Hz and a fluence of 10–12 J/cm<sup>2</sup>. Laser spot size was 40  $\mu\text{m}$ . Carrier gas consisted of purified He plus small quantities of N<sub>2</sub> to minimize oxide formation and increase Hf sensitivity. The data were acquired in static mode with 60-s integrations. Details of analytical procedures and data treatment are after Vervoort et al. (2004) and Dufrene et al. (2007). Mud tank zircon standard ( $^{176}\text{Hf}/^{177}\text{Hf} = 0.282507 \pm 6$ ) (Woodhead & Hergt, 2005) was regularly analyzed between sample blocks to reduce interlaboratory bias and to correct  $^{176}\text{Hf}/^{177}\text{Hf}$  of unknowns. For the Hf-depleted mantle model ages (Hf  $T_{\text{DM}}$ ), we used  $^{176}\text{Hf}/$

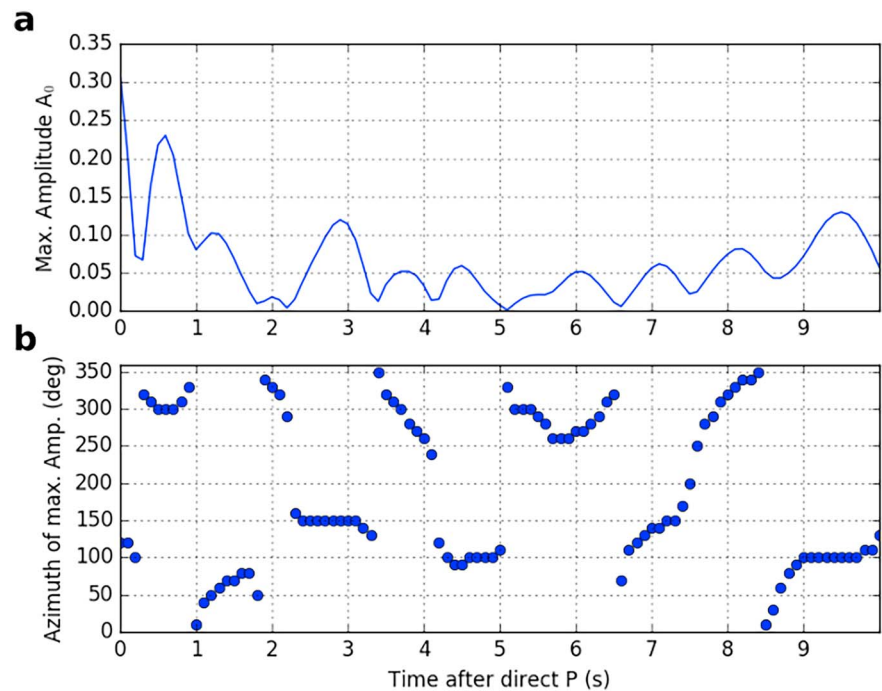


**Figure 5.** Analysis of the behavior of the fitted first azimuthal harmonic with time after P-arrival onset. (a) Maximum amplitude of the degree-1 harmonic function fitted to the receiver function amplitude (vs. back azimuth) at each time point (sampling rate of the receiver functions is 10 samples per second). (b) Azimuth at which the maximum amplitude of the harmonic function occurs at each time point.

$^{177}\text{Hf}$  and  $^{176}\text{Lu}/^{177}\text{Hf}$  for the individual zircon samples to determine their initial  $^{176}\text{Hf}/^{177}\text{Hf}$  ratios at their crystallization ages. Projection back from zircon crystallization was calculated using a present value of 0.0093 for the  $^{176}\text{Lu}/^{177}\text{Hf}$  crust (Amelin et al., 2000; Vervoort & Patchett, 1996). The depleted mantle Hf evolution curve was calculated from present-day depleted mantle values of  $^{176}\text{Hf}/^{177}\text{Hf}$   $\text{DM}_{(0)} = 0.283225$  and  $^{176}\text{Lu}/^{177}\text{Hf}$   $\text{DM}_{(0)} = 0.038512$  (Vervoort & Blichert-Toft, 1999). Results are presented in Table S2.

Whole-rock geochemistry was obtained from four rhyolite samples from the Iza and Paipa volcanic domes; they were analyzed by ICP-MS and inductively coupled atomic emission spectrometry at ALS Minerals Laboratory in Canada. Samples were manually crushed; oxidized and altered surfaces were removed before pulverization in an agate mill. A solution with Lithium metaborate/lithium tetraborate and rock powder was infused in a furnace at 1,000 and 1,025 °C. The resulting melt was cooled and dissolved in 100 ml of an acid mixture containing 4% nitric and 2% hydrochloric acids for inductively coupled atomic emission spectrometry, and nitric, hydrochloric, and hydrofluoric acids for ICP-MS. Results are presented in Table S3.

## 4. Results

### 4.1. Teleseismic Receiver Functions

#### 4.1.1. Eastern Flank of the EC Plateau: Station CHI

From Figures 5 and 6, it can be seen that at 0 s (the time of the first P arrival) and at ~0.6 s, harmonic behavior of the amplitude as a function of back azimuth is clearly apparent (green lines in Figure 6a); the phase difference between them is about 180°. These characteristics of an arrival from depth (P to S conversion out of the source-receiver plane) and its polarity opposite at zero delay (direct P arrival bent at the dipping interface) are consistent with a dipping boundary separating two isotropic layers. Operating with synthetic seismograms, we obtained a plausible response of an interface located at 7 km beneath the station, with an attitude 45/310 (Figure 6b), where wave speed increases with depth. This situation can be consistent with what was obtained with the observed data (Figure 6a). In this area, NW dipping thrusts should be present in the crystalline basement rocks, and it is geologically reasonable to have lower velocity material on top of a higher velocity layer at a depth of 7 km beneath the station; the obtained dip direction is approximately

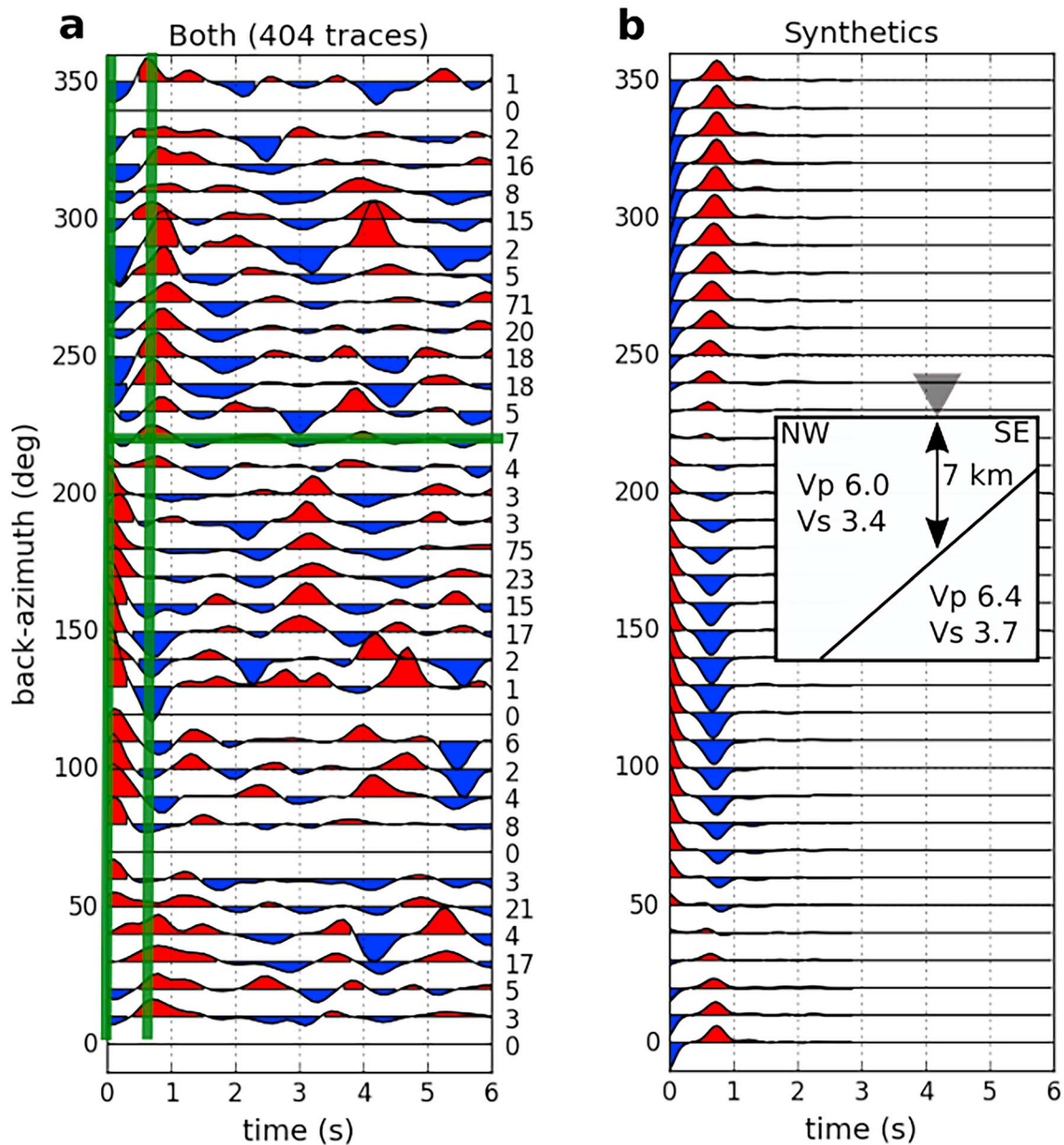


**Figure 6.** Data versus synthetics for Station CHI, at the eastern flank of the Eastern Cordillera. (a) Same as in Figure 4c but with the vertical green lines indicating the time at which the first azimuthal harmonic fitted to the receiver function amplitude reaches its maximum (at 0 and 0.6 s); green horizontal line indicates the approximate strike ( $220^\circ$  or  $N40^\circ E$ ) of the dipping interface, where polarity flips take place and the amplitude of the receiver functions should be close to zero. (b) Synthetics corresponding to a dipping interface with attitude  $45/310$  (dip/dip direction), which separates a low velocity medium on top from a high velocity medium below. Synthetics were generated using the same procedure applied to the data (demeaned radials plus rotated tangentials). Inset shows the sketch of the model used to calculate synthetics; wave speeds are in kilometers per second. Inverted gray triangle represents the station.

perpendicular to the strike of the thrusts in the area (Figure 2), where the Servitá fault is the one that probably controls the structural style of the region (Mora et al., 2008, 2010). The thrusts in the eastern flank of the plateau are expected to merge into a single plane at depth; while it is not clear if that is the interface we are detecting, this major discontinuity is consistent with the known dynamics of thrusting in the area.

#### 4.1.2. Western Flank of the EC Plateau: Station ROSC

Figure 7 suggests that the clearest harmonic behavior in the receiver functions occurs at  $\sim 0.3$  and  $\sim 1.7$  s after the zero-delay P arrival (green lines in Figure 7a); given the separation between both times ( $\sim 1.4$  s), an interface between two isotropic media is unlikely, so an alternative way to generate this pair of harmonic and

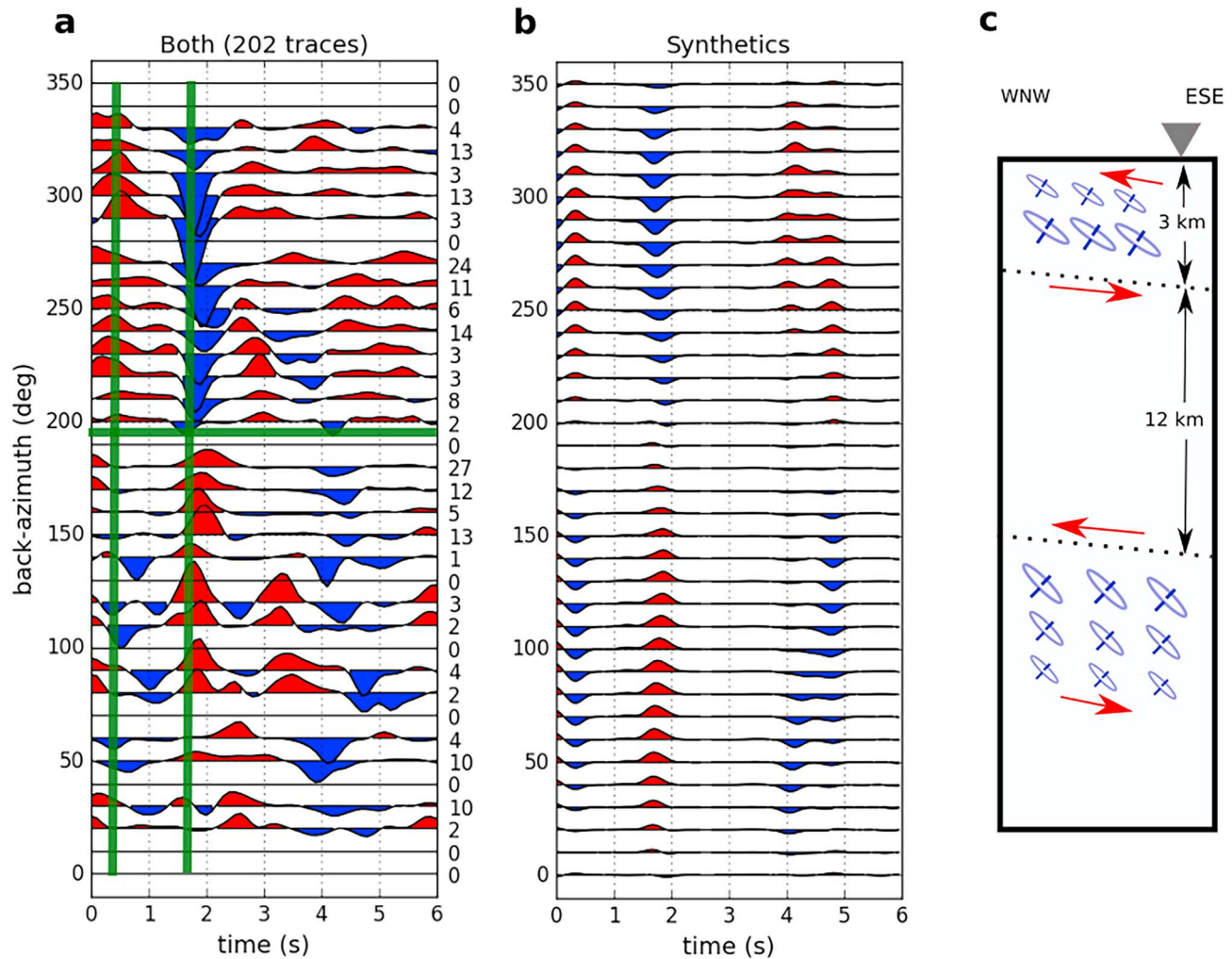


**Figure 7.** Same as in Figure 6 but for Station ROSC, located at the western flank of the Eastern Cordillera. (a) Demeaned radials plus rotated tangentials as a function of back azimuth. (b) Synthetics calculated with the structure indicated in (c), consisting of a ~12-km-thick isotropic layer sandwiched between two layers with gradually varying anisotropy; red arrows illustrate the sense of shear. See text for more description.

anticorrelated azimuthal functions could be the presence of one or several anisotropic layers (Schulte-Pelkum & Mahan, 2014a, 2014b). Given the composition of the crust in the area, the most likely cause of anisotropy is lattice-preferred orientation, with a slow axis symmetry resulting from the orientation of micas (Lloyd et al., 2009; Tatham et al., 2008). In this case, a plausible structure will be a slightly dipping ( $20^{\circ}\text{SE}$ ), ~12 km thick, isotropic layer between two layers with gradually varying anisotropy; the maximum degree of anisotropy would take place near the boundaries between these layers of shear and a relatively stiff isotropic layer. Figure 7b shows the synthetics resulting from this kind of structure, and Figure 7c schematizes the basic geometry. The strength of anisotropy varies between 2% and 8%. The fifth anisotropic parameter, which describes the behavior between symmetry axis and symmetry plane for hexagonal media, is expressed as the shape factor  $\eta$  in the Raysum formulation (Frederiksen & Bostock, 2000). While the value for  $\eta$  is fixed in the original version of Raysum, it should be scaled with the strength of anisotropy (Brownlee et al., 2017; Porter et al., 2011). We used an  $\eta$  value of 0.8, which is consistent with an approximately elliptical anisotropy and with our assumed anisotropy strength range (Brownlee et al., 2017). The strike of the layers of shear is about  $\text{N}10^{\circ}\text{E}$ , so they are parallel to the main thrusts of the western flank (Figure 2), with a slow symmetry axis azimuth of  $110^{\circ}$  and a plunge of  $60^{\circ}$ . Dominant foliation is perpendicular to the symmetry axis, and it is contained within a plane of attitude  $\sim 30/290$  (dip/dip direction), so the strike of the foliation plane is approximately parallel to the thrusts and the mountain range at the western flank ( $\sim 190^{\circ}$ ).

It is known that in this flank of the Cordillera, several thrust systems are superimposed, among which we can highlight the Honda, Cambao, and Bituima Thrusts (Figure 2; Mora et al., 2008); they affect Mesozoic and Cenozoic sedimentary rocks (Mora et al., 2013), creating a layer of shear in the upper 3 km of the crust, where deformation associated to the thrusts concentrates. At the location of Station ROSC, the shallowest levels of the crust corresponds to Cretaceous sedimentary rocks, where nonmarine, transitional, and shallow-marine mudstones predominate (Parra et al., 2009). The base of the anisotropic layer should coincide with the base of the Cretaceous in the area, which constitutes a major unconformity in the region (Parra et al., 2009). In the outcropping Early Cretaceous rocks of the EC, mineral fabric has developed, and low grade metamorphism has been documented (Silva-Arias et al., 2010), so it is plausible that micas are responsible for anisotropy. Even though a depth of 3 km is too shallow to develop mineral fabric, balanced cross sections in the area indicate that the base of the Cretaceous has been uplifted/exhumed nearly 8–10 km in the process of shortening/thrusting during the Cenozoic (Cortés et al., 2006; Mora et al., 2013) so that the fabric generation occurred several kilometers deeper.

The stratigraphic record of pre-Cretaceous age in the area corresponds mostly to Jurassic sandstones (Parra et al., 2009), Paleozoic sedimentary rocks among which sandstones and conglomerates predominate (Kammer, 1996; Renzoni, 1967), and the crystalline basement, which consists of low and medium grade metamorphic continental rocks and intermediate to acid intrusives (Parra et al., 2009). These coarser pre-Cretaceous materials are likely to constitute a stiff and relatively thick (~12 km) layer. The lower shear zone may have developed in the predominant chlorite schists and phyllites that have been documented in the outcropping basement; the ESE dip of the shear layer at a depth of ~15 km beneath Station ROSC is consistent with the hypothesis of a shallowly dipping major thrust fault cutting through the basement, as it has been suggested in the reconstructions of Cortés et al. (2006) and Mora et al. (2013). In general, the generation of several shear zones with gradual variations in mica fabric is consistent with the style of deformation in the area, where shortening has been absorbed mostly along thrust faults that affect the sedimentary rocks and possibly the crystalline basement.

#### 4.1.3. Region of the Volcanic Domes: Station RUS

Results at broadband Station RUS suggest a cyclic behavior of the receiver function amplitude versus back azimuth at 0 and ~0.4 s after the first P arrival (green lines in Figure 8a). This segment of the record is consistent with a dipping boundary separating two isotropic media with velocity contrast (Schulte-Pelkum & Mahan, 2014a, 2014b). Synthetics resulting from a dipping boundary (35/320) at 5 km beneath the station, with a slow layer beneath a fast layer (a plausible situation at shallow crustal levels in a region of active thrusting), are shown in Figures 8b and 8c. In this region, Jurassic, Cretaceous, and Paleogene units are overthrusting Neogene units (Kammer, 1996); Paleozoic basement also overlies Paleozoic and Mesozoic sedimentary rocks in this area (Mora et al., 2013). The mapped boundary and the thrust faults in the area seemingly share the same attitude, making this a plausible interpretation of the data.

Of special interest is the large amplitude of the first azimuthal harmonic at about 4.5 s (Figure 8a, black box). It suggests that there should be a significant boundary in the lower crust beneath the area of volcanism associated with the Paipa and Iza domes (Figure 2). We use synthetics to model the data for the case where there is a lower crustal interface with a high velocity layer at the bottom of the crust; Figure 8b shows the response of a slightly dipping interface (10°/20°, strike/dip) at about 36 km beneath the station (Figure 8c) that represents a lower crustal major boundary with a high velocity layer at the bottom of the crust. There is some level of noise in the data at this time interval (Figure 8a, black box), but the acceptable fit to a harmonic function (Figures 8a and 8b) suggests this to be a plausible interpretation (Schulte-Pelkum & Mahan, 2014a, 2014b). This boundary at about 36 km beneath the station is too shallow to be the Moho (Poveda et al., 2015; see Figure S1 for the averaged radial receiver functions including times that show the deeper presumed Moho conversion), and the base of the crust in this area may represent underplated material from the mantle or a lower crustal magmatic intrusion (Thybo & Artemieva, 2013).

## 4.2. Geochronology and Geochemistry

### 4.2.1. U-Pb and Hf Zircon Geochronology

U-Pb laser ablation-ICP-MS zircon ages were found for a rhyolitic dyke (analytical results and age calculations are presented in Table S1). Zircons are characterized by sizes between 150 and 400  $\mu\text{m}$  with prismatic habit and length/wide ratios of 2:1 (Figure 9a). Cathodoluminescence images show single oscillatory zoning

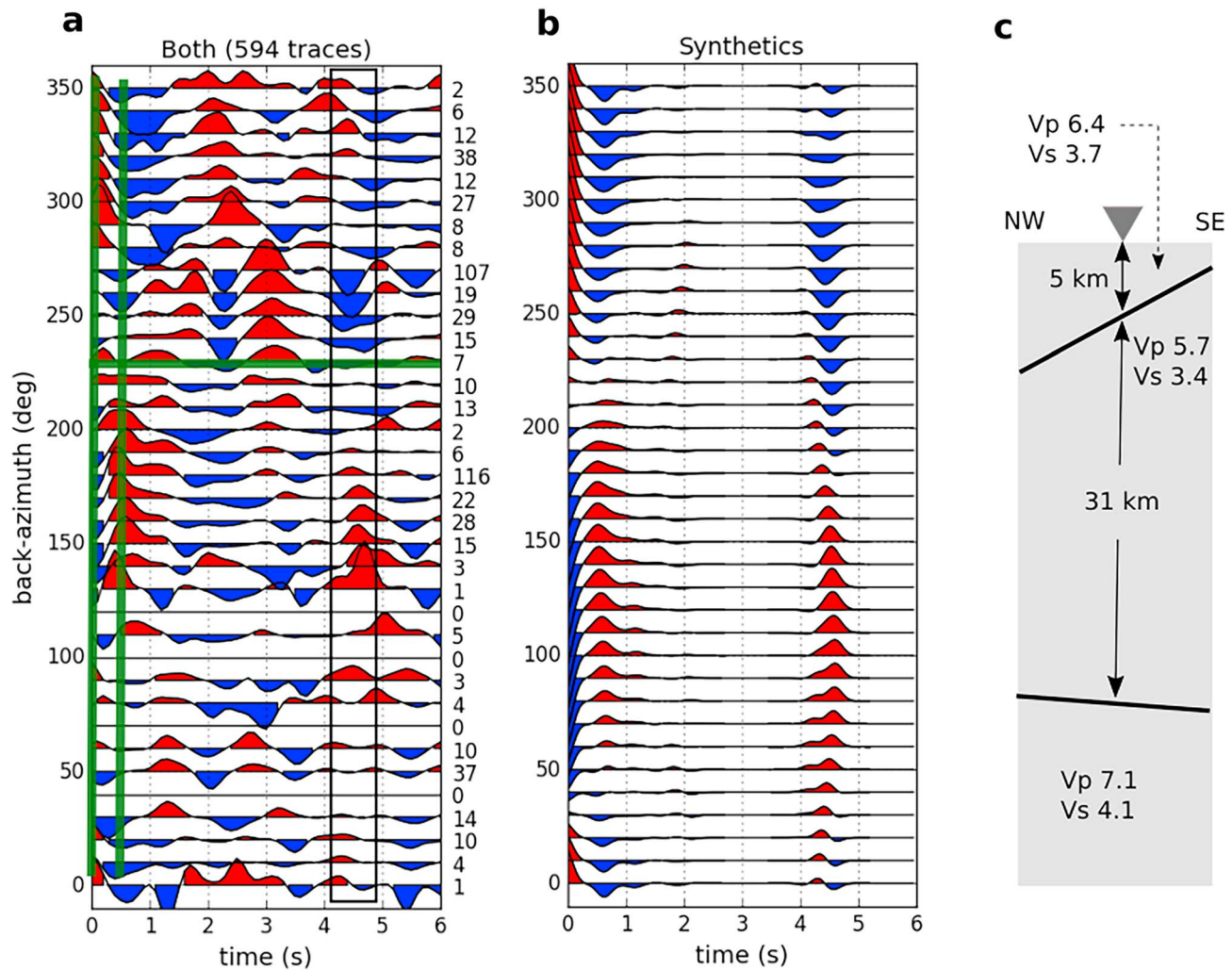


**Figure 8.** Same as in Figures 6 and 7 but for Station RUS, located at the northern part of the Eastern Cordillera plateau. (a) Demeaned radials plus rotated tangentials as a function of back azimuth. (b) Synthetics. Black box encloses the amplitude signature of a possible lower crustal interface (see text for explanation). (c) Sketch of the structure used to calculate the synthetics in (b); seismic speeds are in kilometers per second.

in zircons as well as core zircon crystals with overgrown rims also with an oscillatory zoning pattern, characteristic of igneous zircons (Corfu et al., 2003). The Th/U ratio of the 30 analyzed zircon crystals varies between 0.17 and 0.40, which are characteristic values of magmatic-derived zircons (Rubatto, 2002). Zircons yielded a weighted average age of 5.9 Ma with a propagated error ( $2\sigma$ ) of 0.1 Ma (Figure 9a), which is considered as the magmatic crystallization age. Some cores with associated rims as well as isolated crystals yielded crystallization ages between 380 and 1,032 Ma, which were interpreted as reworked zircons from the host sedimentary rocks. Initial  $^{176}\text{Hf}/^{177}\text{Hf}$  ratio from the 30 Late Miocene zircons varies between 0.282613 and 0.282726 with negative values of initial  $\epsilon\text{Hf}$  between  $-6.0$  and  $-2.0$  (Figure 9b), which are characteristic of an older crustal input.

#### 4.2.2. Whole Rock Geochemistry

In this section we integrate previously published whole rock geochemical results with four new results obtained for the regions of the Paipa (2) and Iza (2) domes (Figure 2). From the Iza region, we have included eight samples analyzed by Vesga and Jaramillo (2009), for which both major and trace elements were determined. We have discarded three samples from these authors that have  $\text{SiO}_2$  values higher than 80% and trace element patterns that are not characteristic of magmatic rocks. For the Paipa region, we have included the whole rock major element data presented by Pardo, Jaramillo, et al. (2005). None of the previously published results reports lost on ignition (LOI) values; the two new samples from Iza are characterized by contrasting LOI values between 2.6% and 18.9%, whereas in Paipa, they are 1.2% and 3.6%.

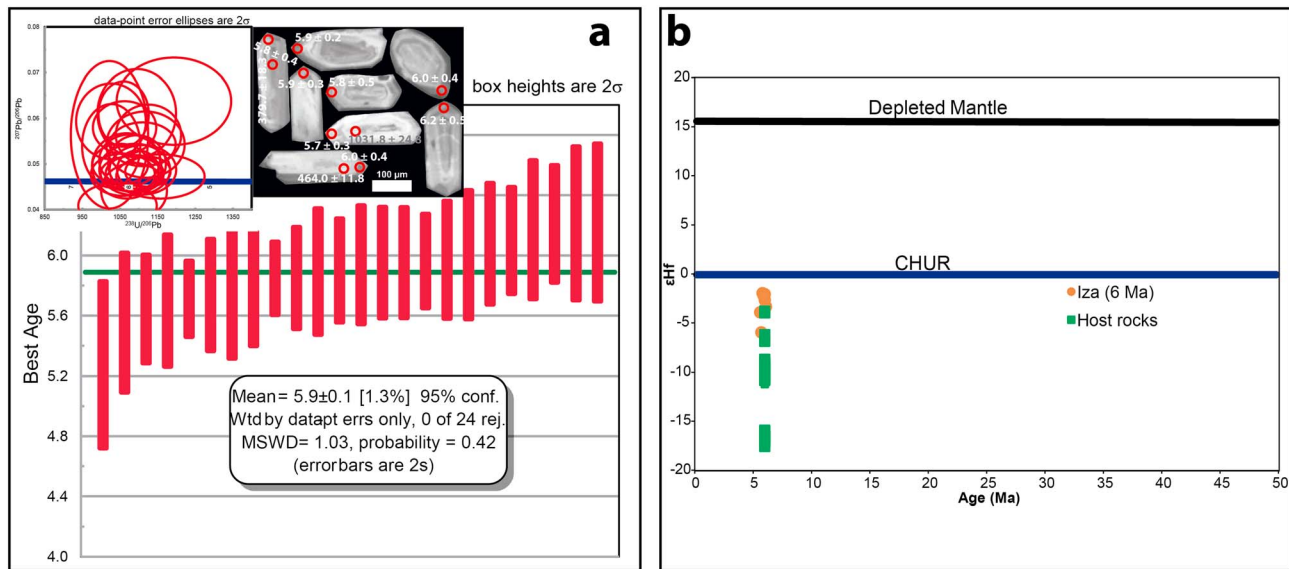


**Figure 9.** U-Pb geochronological plots from Iza volcano. (a) Weighted average age including Tera-Wasserburg diagram and cathodoluminescence images from zircons. (b) Hf isotopes compared with host rocks. MSWD = mean square weighted deviation.

Both volcanic centers are characterized by similar major element compositional characteristics, with  $\text{SiO}_2$  values between 51.7% and 72.2% and total alkalis ( $\text{Na}_2\text{O} + \text{K}_2\text{O}$ ) between 1.5% and 11.6%;  $\text{Fe}_2\text{O}_3$  varies between 0.5 and 3.7 Wt%, whereas the more immobile  $\text{TiO}_2$  and  $\text{P}_2\text{O}_5$  vary between 0.2% and 0.6% and 0.13% and 0.18%, respectively. Due to the LOI values of the analyzed samples and the lack of correlation between Zr and most of the major elements, we will mostly concentrate on trace elements.

Using the immobile elements that considered Nb/Y and Zr/Ti as the silica and alkaline indexes (Winchester & Floyd, 1977; modified by Pearce, 1996), the rocks are classified between dacite-rhyolite and tephryphonolite (Figure 10a); this is similar to what is seen in Th-Co (Hastie et al., 2007; Figure 10b) that also suggested that the samples are in the calc-alkaline and the high potassium shoshonitic series. Considering the tectonic discrimination diagrams for felsic and intermediate volcanic rocks after Gorton and Schandl (2000), samples are characterized by an intraplate to convergent margin signature (Figure 10c).

Two different compositional groups are separated with the Rare Earth Elements (REE), Zr, Ti, and Nb. Samples from Iza are characterized by lower Heavy REE contents when compared with Paipa; they have Light REE enrichment, with  $(\text{La}/\text{Sm})_n$  ratios between 4.2 and 8.2,  $(\text{La}/\text{Yb})_n$  ratios between 1.1 and 26.5, and a flat to negative slope between the Middle and Heavy REE ( $(\text{Gd}/\text{Yb})_n$  ratios between 0.2 and 1.2). They show a U-like shape and a well-defined Eu negative anomaly (Figure 10d), with  $\text{Eu}/\text{Eu}^*$  values between 0.7 and 1.2, whereas the multielement diagrams show a relatively low value of Nb and an absence of a negative Ti anomaly (Figure 10e). REE patterns from the Paipa region are characterized by similar Light REE enrichment with  $(\text{La}/\text{Sm})_n$  ratios between 4.7 and 7.1 but lower  $(\text{La}/\text{Yb})_n$  ratios between 6.5 and 16.8; they are also characterized by flat to negative slopes between the Middle and Heavy REE, with  $(\text{Gd}/\text{Yb})_n$  ratios between 0.9 and 1.3, and by well-defined Eu anomalies, with  $\text{Eu}/\text{Eu}^*$  values between 0.6 and 0.7 (Figure 10d). Multielement patterns indicate a low value of Nb and a strong negative Ti anomaly (Figure 10e).

## 5. Discussion and Tectonic Implications

Our observations, which include geophysical and geochemical methods, are consistent with two main mechanisms that may be responsible for crustal thickening (thickness values between 46 and 60 km) in the EC of Colombia: shortening during the Cenozoic and consequent reaccommodation of masses and magmatic underplating as a result of partial melt in the mantle. In the next paragraphs we discuss these two mechanisms and how our findings support their prevalent role in the construction of the present EC.

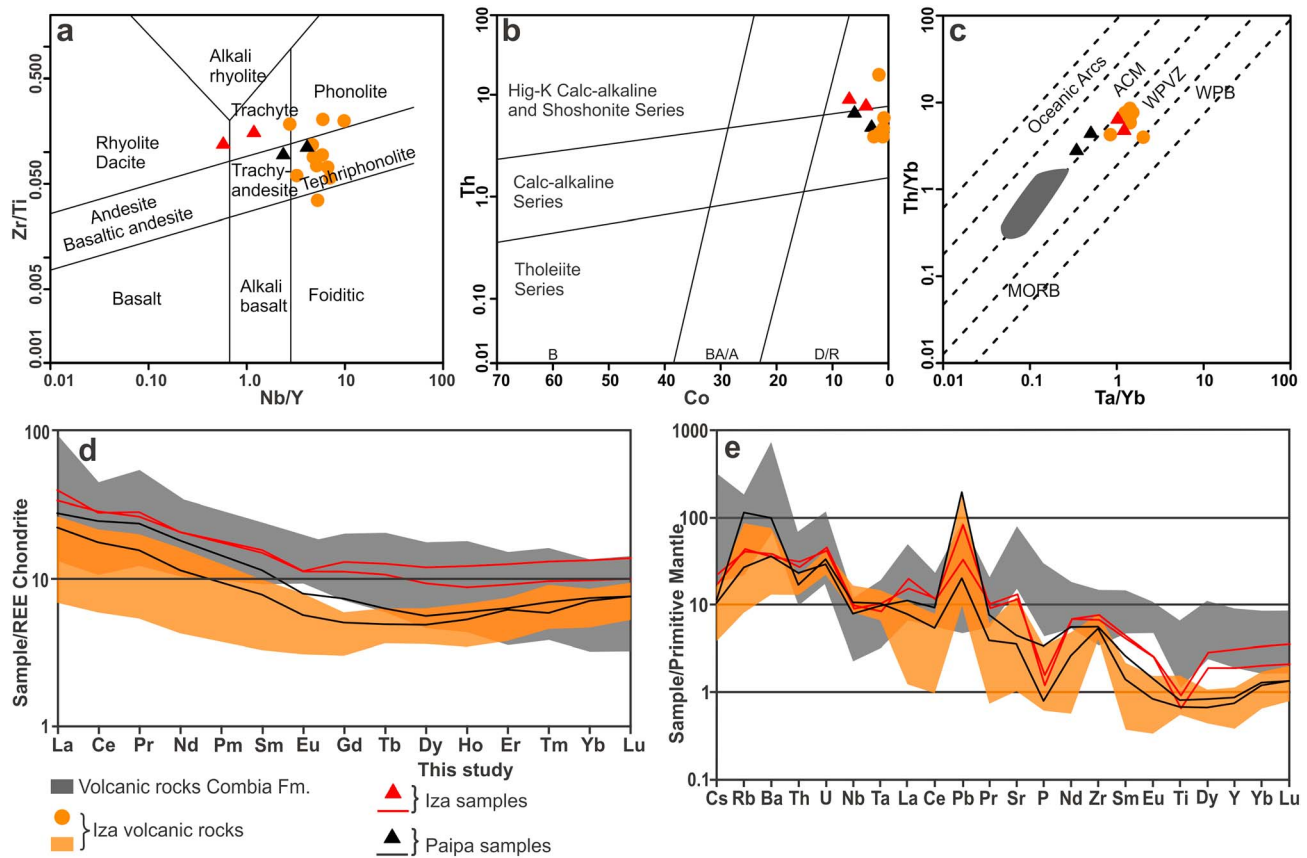


**Figure 10.** Geochemical analyses for samples of the present and previous studies. (a) Classification diagram of Winchester and Floyd (1977); modified by Pearce, 1996). (b) Co-Th classification diagram (Hastie et al., 2007). (c) Gorton and Schandl (2000) geotectonic diagram. In addition to results from the present study, we include Iza volcano published data (Vesga & Jaramillo, 2009) and coetaneous upper Miocene volcanic rocks from Combia Formation (Rodríguez & Zapata, 2014); note the consistency of the results of Vesga and Jaramillo (2009) with those from this study (red and black triangles). Spider diagrams in (d) and (e) show our results for Iza and Paipa volcanoes and a comparison with Iza volcano published data (Vesga & Jaramillo, 2009) and data from coetaneous Upper Miocene volcanic rocks from Combia Formation (Rodríguez & Zapata, 2014). (a) Rare earth elements normalized to Chondrite (Nakamura, 1974). (b) Multi-elemental diagram normalized to Primitive Mantle (McDonough & Sun, 1995). ACM = Active Continental Margin; WPVZ = within-plate volcanic zone; WPB = within-plate alkali basalt; MORB = mid-oceanic-ridge basalt.

The seismic lines analyzed up to date (e.g., Mora et al., 2008, 2010, 2013; Parra et al., 2012) contain very detailed information of the configuration at several locations, but they might be insufficient to provide enough information about the most significant features at a crustal scale. Using receiver functions, we can find evidence for structures that describe larger-scale geometry of the crust, compared with the localized details available seismic lines can provide. The major interfaces proposed in this study in the EC are consistent with shortening being absorbed on major crustal thrust faults and with the generation of duplexes. The presence of anisotropic layers at several levels within the crust beneath the western flank is consistent with substantial shearing taking place during the deformation process that has built the cordillera (Montes et al., 2005).

Results presented in Figure 6 (CHI) and 7 (ROSC) suggest different structural styles at both flanks of the cordillera. On the eastern flank (Station CHI, Figure 6), receiver functions indicate that the most notable upper crustal feature is an isotropic NW dipping interface that may juxtapose crystalline basement rocks, likely with damage concentrated in the low-velocity wall; on the other hand, on the western flank (Station ROSC, Figure 7), we find evidence for at least two anisotropic layers resulting from localized shear. The process of thrusting during the Cenozoic has uplifted Paleozoic and Mesozoic sedimentary rocks; it is unclear whether the basement has been uplifted, but it is certainly plausible that thrusting contributed to the development of mineral fabric.

Early Cretaceous fine-grained sedimentary units in the shallowest crust of the EC have evolved to low grade metamorphic rocks, and the suggested presence of mineral fabric in the western flank may be an expression of localized shear associated with shortening. The stratigraphic and structural record of this flank suggests that the thrusting that built the present configuration of the EC took place during the Neogene, as Cretaceous units are on top of Miocene sedimentary rocks; the metamorphic fabric may have developed at this stage, but we cannot rule out the possibility that deformation in the early Cenozoic and the late Cretaceous resulted in low grade metamorphism. The deeper shear zone (Figure 7c) may have developed in the phyllites and schists of the metamorphic basement (Renzoni, 1967), below stiffer materials of the basement and Paleozoic and Jurassic predominantly coarse-grained rocks; the time of deformation is also uncertain, as well as its association with the shortening that largely contributed to the formation of the modern EC.

Our receiver function analysis also suggests the existence of high density and high seismic velocity (mafic) material in the lower crust below the Paipa-Iza region (~36 km below the surface), which may represent underplated mafic magmas from which the intermediate to felsic volcanic rocks on the surface were derived. The origin and implications of magmatism in the EC has not been extensively addressed, and most of the discussions are restricted to their emplacement associated with deep faults (Bernet et al., 2016). We therefore placed the geophysical, geochronological, and geochemical constraints within a series of regional tectonic restrictions to explore the bearing of this record on the Cordilleran tectonics: (1) Despite the controversies surrounding the limit between Nazca and Caribbean subduction, the seismicity pattern leads us to assume that the Paipa-Iza segment of the Cordillera is related to Nazca subduction (Chiarabba et al., 2016; Syracuse et al., 2016; Wagner et al., 2017), with the trench located ~570 km to the west. (2) Although modern arc volcanism is absent at this latitude, by 5–6 Ma, the arc front was active ~270 km to the west, in the Cauca Valley (Wagner et al., 2017), between the Western and Central Cordilleras (Figure 1). (3) Between the late Miocene and Pliocene, the EC was experiencing compression (Mora et al., 2010, 2015).

The intermediate to felsic volcanic Mio-Pliocene rocks from the Iza and Paipa regions are characteristic of a high-K shoshonite to alkaline character (Figure 10b). High-K magmatism has been documented in the distal continentward side of volcanic arcs (Guillot et al., 2011; Kay & Mpodozis, 2002), and its origin has been related to either crustal or subcontinental mantle melting or to deeper mantle melting. The Mesozoic tectonomagmatic history recorded in the EC rocks may include an older Jurassic arc or rift-related record (Mantilla-Figueroa et al., 2013; Van der Lelij et al., 2016), followed by a major Cretaceous extensional phase that must have reduced the thickness of the former subduction related metasomatized mantle (Vásquez et al., 2010; Vásquez & Altenberger, 2005), therefore limiting the influence of an inherited subduction-related signature on the Mio-Pliocene magmatism in the EC.

The enrichment in the Light REE relative to the Heavy REE, the relatively low Nb value in the spider diagram (Figure 10e), and the calc-alkaline to shoshonite trend are characteristics of convergent margins in which the mantle was being modified by some input from slab-related fluids so that this volcanism must be related to a Cenozoic event. Trace element ratios and tectonic discrimination diagrams have shown that the alkaline to shoshonite trend is characterized by both arc (Paipa and Iza) and intraplate (Iza) signatures, which is indicative of moderate Th crustal contamination (Gorton & Schandl, 2000); this is also suggested by Nb/La values between 0.4 and 0.5 for Paipa and 0.7 and 3.3 for Iza. These numbers indicate that the later may have a stronger crustal input (Li et al., 2017), which is also supported by the negative pattern of the  $\epsilon_{\text{Hf}}$  signature (Figure 9b).

We therefore suggest that the source of the lower crust mafic magmatism is the melt of a weakly enriched subcontinental mantle. Melting of the lithospheric or asthenospheric mantle in convergent margins may be either related to delamination after considerable crustal thickening, which may be commonly associated with extension (Kay & Kay, 1993), or to changes in the subduction angle (Kay et al., 2006; Kay & Mpodozis, 2002). For the EC, we favor shallowing of the slab as the main trigger mechanism, as neither the temporal association of this magmatism with compression (Mora et al., 2010, 2015) nor the relatively uniform lithospheric thickness in the whole northern Andes region (Blanco et al., 2017) fit the delamination hypothesis. As the slab angle shallows, asthenospheric upwelling can trigger lithospheric melting (Li & Li, 2007).

Relatively recent arc magmatism documented ~270 km to the west of the EC, denominated Combia magmatism (Jaramillo et al., 2019; Rodríguez & Zapata, 2014), has a clear signature of subduction (Figure 10), clearly differing from the EC. Considering that the oldest ages of the Paipa-Iza volcanics coincide with the

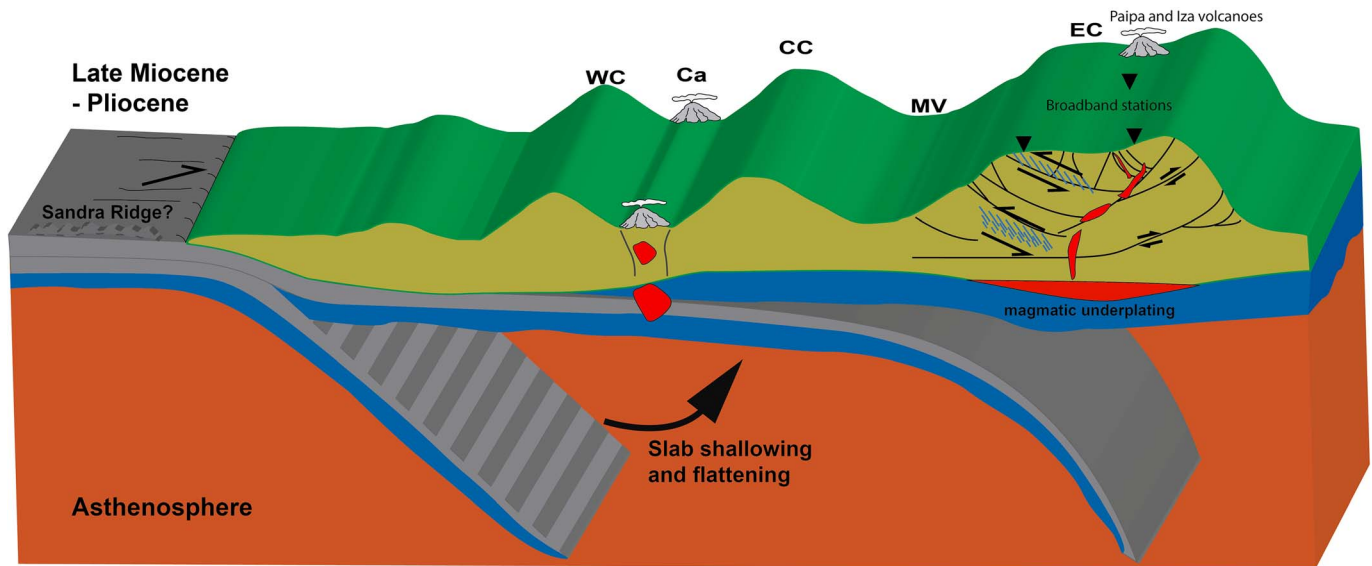


**Figure 11.** Schematic representation (not to scale) of our main hypotheses. The Nazca-slab shallowing and flattening, together with the compressional regime acting on the EC during the Cenozoic, can explain the crustal thickening and uplift, as well as the observed magmatism. Local magmatic underplating is consistent with the receiver functions results (Figure 8). The patterns of gray dipping lines beneath the western side of the EC indicate mineral fabric, as suggested by the receiver function results (Figure 7). Red colors are indicative of magmatism. Since our emphasis was in the EC, we do not sketch structures beneath the CC, WC, nor other domains. WC = Western Cordillera; CC = Central Cordillera; EC = Eastern Cordillera; Ca = Cauca arc (Combia magmatism); MV = Magdalena Valley.

youngest ones of the Combia magmatism (5–6 Ma), it is plausible to hypothesize that at that time, the latter was vanishing, and the slab started flattening; partial melting in the mantle related with this flattening may have caused magmatism in the EC, taking place in an intraplate position as a consequence of readjustments in the subducted slab. Seismicity, tomographic imaging, and the evaluation of the spatial distribution of magmatic rocks in the Colombian Andes (Chiarabba et al., 2016; Syracuse et al., 2016; Vargas & Mann, 2013; Wagner et al., 2017) support the existence of a modern flat slab setting north of  $\sim 5.5^\circ\text{N}$ . Therefore, we propose that the magmatic record of the EC, which is north of this latitude, is linked to the flat slab configuration that also triggers the Pliocene uplift and exhumation. This hypothesis agrees with recent findings of Siravo et al. (2018), who gave evidence in the eastern flank of the EC for metamorphic overprints and signs of thermal perturbations in ZHe ages that are consistent with local magmatic intrusions in the late Miocene. In addition, modeling results presented by Siravo et al. (2019) suggest that slab shallowing and flattening between  $\sim 10$  and  $\sim 6$  Ma can explain the EC topography and can account for the fast exhumation in the Plio-Pleistocene; they argue that if the asthenospheric wedge is hydrated enough, the slab flattening may be responsible for the topographic uplift of the EC.

Receiver functions at Station RUS (Figure 8) are consistent with basaltic melts emplaced in the lower crust that experienced differentiation and some crustal assimilation, as suggested by variations from intermediate to felsic compositions. The low V (22–63 ppm) and Ni contents (0.1–9 ppm) when compared to Zr are characteristics of fractional crystallization (Li et al., 2017; Peccerillo et al., 2003). The concave middle Rare Earth Element pattern (Figure 10d) indicates that fractionation may have taken place in the amphibole stability field (Tiepolo & Tribuzio, 2008), which is also compatible with the 36-km depth of the magmatic underplating. Variations between the arc and within-plate signature, including the changes in the Ti anomaly, the  $\epsilon\text{Hf}$ , and the presence of older cores with 5.9-Ma rims, may be associated with variable crustal assimilation as the magmas are emplaced at shallow crustal levels. Finally, the ascent of the melt may have been facilitated by the presence of crustal-scale reactivated faults.

Our main hypotheses about the building of the EC Plateau, including the Nazca slab shallowing and flattening in the late Miocene-Pliocene, are summarized in Figure 11. Shortening during the Cenozoic has been absorbed in reactivated high angle faults and regional thrusts; deformation since the early Cenozoic in the western flank has contributed to the generation of foliation within the crust, manifested in the systematic orientation of minerals at several levels. Magmatic additions have also played a role in crustal thickening;

magmas have been emplaced at the bottom of the crust and have ascended through crustal faults. Slab shallowing and flattening in the late Miocene-Pliocene could have triggered exhumation and uplift (Siravo et al., 2019), as well as the magmatic processes.

## 6. Conclusions

The present crustal configuration beneath the plateau of the EC of Colombia, where Moho depths vary between ~46 and 60 km, appears to be the result of shortening in a fold-and-thrust belt controlled by regional faults and of magmatic underplating, which constitute plausible mechanisms for crustal thickening in the area. The EC has been under compression since the beginning of the Cenozoic. Teleseismic receiver functions may be revealing a signature of the resulting shortening (and thickening), expressed in stacked shear zones within the crust and major intracrustal faults; such features accommodate a large portion of the induced deformation.

The presence of a seismically fast layer in the lower crust beneath the region of the Paipa and Iza volcanic domes is consistent with magmatic underplating. The geochemical characteristics of the rocks that outcrop in the area of the volcanic domes, which yielded ages of ~5.9 Ma and younger, suggest that partial melt occurred in the upper mantle; the resulting magmas may have been added to the crust by underplating, and small portions of them may have ascended through the crust along crustal-scale faults and undergone differentiation and crustal assimilation. We argue that the EC magmatism is related to the shallowing of the subduction angle, a process that should have been active by ~6 Ma.

## Acknowledgments

The authors would like to thank the Colombian science foundation COLCIENCIAS for the 2-year support through Grant 50491. The azimuthal receiver function analysis method was developed under U.S. National Science Foundation Grants EAR-1251193 and 1735890. Special thanks to Servicio Geológico Colombiano (SGC) for sharing the seismological data. Reviews by Camilo Montes and an anonymous referee greatly helped improve the quality of the manuscript. The raw broadband waveforms used to calculate the receiver functions are available online (<https://doi.pangaea.de/10.1594/PANGAEA.905109>).

## References

- Alfaro, C., Velandia, F., Cepeda, H., & Pardo, N. (2010). Preliminary conceptual model of the Paipa geothermal system, Colombia. *Proceedings of the World Geothermal Congress, Bali, Indonesia*, 7pp.
- Amelin, Y., Lee, D. C., & Halliday, A. N. (2000). Early-Middle Archaean crustal evolution deduced from Lu-Hf and U-Pb isotopic studies of single zircon grains. *Geochimica et Cosmochimica Acta*, 64(24), 4205–4225. [https://doi.org/10.1016/S0016-7037\(00\)00493-2](https://doi.org/10.1016/S0016-7037(00)00493-2)
- Anderson, V. J., Saylor, J. E., Shanahan, T. M., & Horton, B. K. (2015). Paleoelevation records from lipid biomarkers: Application to the tropical Andes. *Geological Society of America Bulletin*, 127(11–12), 1604–1616. <https://doi.org/10.1130/B31105.1>
- Babault, J., Teixell, A., Struth, L., van den Driessche, J., Arboleya, M. L., & Tesón, E. (2013). Shortening, structural relief and drainage evolution in inverted rifts: Insights from the Atlas Mountains, the Eastern Cordillera of Colombia and the Pyrenees. In M. Nemcok, A. Mora, & J. W. Cosgrove (Eds.), *Thick-skin dominated orogens: From initial inversion to full accretion, Special Publication (Vol. 377, 141–158)*. London: Geological Society. <https://doi.org/10.1144/SP377.14>
- Bayona, G., Cardona, A., Jaramillo, C., Mora, A., Montes, C., Caballero, V., et al. (2013). Onset of fault reactivation in the Eastern Cordillera of Colombia and proximal Llanos Basin; response to Caribbean–South American convergence in early Palaeogene time. In M. Nemcok, A. Mora, & J. W. Cosgrove (Eds.), *Thick-skin dominated orogens: From initial inversion to full accretion, Special Publications (Vol. 377, pp. 411–442)*. London: Geological Society. <https://doi.org/10.1144/SP377.5>
- Bernet, M., Uruña, C., Amaya, S., & Peña, M. L. (2016). New thermo and geochronological constraints on the Pliocene-Pleistocene eruption history of the Paipa-Iza volcanic complex, Eastern Cordillera, Colombia. *Journal of Volcanology and Geothermal Research*, 327, 299–309. <https://doi.org/10.1016/j.jvolgeores.2016.08.013>
- Blanco, J. F., Vargas, C. A., & Monsalve, T. G. (2017). Lithospheric thickness estimation beneath Northwestern South America from an S-wave receiver function analysis. *Geochemistry, Geophysics, Geosystems*, 18, 1376–1387. <https://doi.org/10.1002/2016GC006785>
- Brownlee, S. J., Schulte-Pelkum, V., Raju, A., Mahan, K., Condit, C., & Orlandini, O. F. (2017). Characteristics of deep crustal seismic anisotropy from a compilation of rock elasticity tensors and their expression in receiver functions. *Tectonics*, 36, 1835–1857. <https://doi.org/10.1002/2017TC004625>
- Cediel, F., Shaw, R. P., & Caceres, C. (2003). Tectonic assembly of the Northern Andean Block. In *The circum-gulf of Mexico and the Caribbean: Hydrocarbon habitats, basin formation, and plate tectonics, AAPG Memoir (Vol. 79, pp. 1–34)*.
- Chang, Z., Vervoort, J. D., McClelland, W. C., & Knaack, C. (2006). U-Pb dating of zircon by LAICP-MS. *Geochemistry, Geophysics, Geosystems*, 7, Q05009. <https://doi.org/10.1029/2005GC001100>
- Chiarabba, C., De Gori, P., Faccenna, C., Speranza, F., Seccia, D., Dionicio, V., & Prieto, G. A. (2016). Subduction system and flat slab beneath the Eastern Cordillera of Colombia. *Geochemistry, Geophysics, Geosystems*, 17, 16–27. <https://doi.org/10.1002/2015GC006048>
- Corfu, F., Hancher, J. M., Hoskin, P. W. O., & Kinny, P. (2003). Atlas of zircon textures. *Reviews in Mineralogy and Geochemistry*, 53(1), 469–500. <https://doi.org/10.2113/0530469>
- Corredor, F. (2003). Eastward extent of the Late Eocene-Early Oligocene onset of deformation across the northern Andes: Constraints from the northern portion of the Eastern Cordillera fold belt, Colombia. *Journal of South American Earth Sciences*, 16(6), 445–457. <https://doi.org/10.1016/j.jsames.2003.06.002>
- Cortés, M., Colletta, B., & Angelier, J. (2006). Structure and tectonics of the central segment of the Eastern Cordillera of Colombia. *Journal of South American Earth Sciences*, 21(4), 437–465. <https://doi.org/10.1016/j.jsames.2006.07.004>
- Dufrane, S. A., Vervoort, J. D., & Hart, G. L. (2007). Uncertainty of Hf isotope analysis in zircon using LA-MC-ICPMS techniques: Full disclosure, 17th annual V.M. Goldschmidt Conference, Cologne, Germany. *Geochimica et Cosmochimica Acta*, 71, A241.
- Frederiksen, A. W., & Bostock, M. G. (2000). Modelling teleseismic waves in dipping anisotropic structures. *Geophysical Journal International*, 141(2), 401–412. <https://doi.org/10.1046/j.1365-246x.2000.00090.x>

- Gómez, E., Jordan, T. E., Allmendinger, R. W., Hegarty, K., Kelley, S., & Heizler, M. (2003). Controls on architecture of the Late Cretaceous to Cenozoic southern Middle Magdalena Valley Basin, Colombia. *Geological Society of America Bulletin*, *115*, 131–147. <https://doi.org/10.1130/0016-7606>
- Gorton, M. P., & Schandl, E. S. (2000). From continents to island arcs: A geochemical index of tectonic setting for arc-related and within-plate felsic to intermediate volcanic rocks. *The Canadian Mineralogist*, *38*(5), 1065–1073. <https://doi.org/10.2113/gscanmin.38.5.1065>
- Guillot, M. G., Escayola, M., & Acevedo, R. (2011). Calc-alkaline rear-arc magmatism in the Fuegian Andes: Implications for the mid-Cretaceous tectonomagmatic evolution of southernmost South America. *Journal of South American Earth Sciences*, *31*(1), 1–16. <https://doi.org/10.1016/j.jsames.2010.11.002>
- Hastie, A. R., Kerr, A. C., Pearce, J. A., & Mitchell, S. F. (2007). Classification of altered volcanic island arc rocks using immobile trace elements: development of the Th-Co discrimination diagram. *Journal of Petrology*, *48*(12), 2341–2357. <https://doi.org/10.1093/petrology/egm062>
- Hincapié-Gómez, S., Cardona, A., Jiménez, G., Monsalve, G., Ramírez-Hoyos, L., & Bayona, G. (2018). Paleomagnetic and gravimetric reconnaissance of Cretaceous volcanic rocks from the Western Colombian Andes: Paleogeographic connections with the Caribbean Plate. *Studia Geophysica et Geodaetica*, *62*(3), 485–511. <https://doi.org/10.1007/s11200-016-0678-y>
- Horton, B. K., Saylor, J. E., Nie, J. S., Mora, A., Parra, M., Reyes-Harker, A., & Stockli, D. F. (2010). Linking sedimentation in the northern Andes to basement configuration, Mesozoic extension, and Cenozoic shortening: Evidence from detrital zircon U-Pb ages, Eastern Cordillera, Colombia. *Geological Society of America Bulletin*, *122*(9–10), 1423–1442. <https://doi.org/10.1130/B30118.1>
- Irving, E. (1971). *La evolución estructural de los Andes más septentrionales de Colombia* (Vol. 19, p. 90). Bogota: Boletín Geológico Colombiano – Instituto Nacional de Investigaciones Geológico Mineras.
- Jaramillo, J. S., Cardona, A., Monsalve, G., Valencia, V., & León, S. (2019). Petrogenesis of the late Miocene Combia volcanic complex, northwestern Colombian Andes: Tectonic implication of short term and compositionally heterogeneous arc magmatism. *Lithos*, *330–331*, 194–210. <https://doi.org/10.1016/j.lithos.2019.02.017>
- Kammer, A. (1996). Estructuras y deformaciones del borde oriental del macizo de Floresta. *Geologia Colombiana*, *21*, 65–80.
- Kay, R. W., & Kay, S. M. (1993). Delamination and delamination magmatism. *Tectonophysics*, *219*(1–3), 177–189. [https://doi.org/10.1016/0040-1951\(93\)90295-U](https://doi.org/10.1016/0040-1951(93)90295-U)
- Kay, S. M., Burns, W. M., Copeland, P., & Mancilla, O. (2006). Upper Cretaceous to Holocene magmatism and evidence for transient Miocene shallowing of the Andean subduction zone under the northern Neuquén Basin. *Special paper of the Geological Society of America*, *407*, 19–60. [https://doi.org/10.1120/2006.2407\(02\)](https://doi.org/10.1120/2006.2407(02))
- Kay, S. M., & Mpodozis, C. (2002). Magmatism as a probe to the Neogene shallowing of the Nazca plate beneath the modern Chilean flat-slab. *Journal of South American Earth Sciences*, *15*(1), 39–57. [https://doi.org/10.1016/S0895-9811\(02\)00005-6](https://doi.org/10.1016/S0895-9811(02)00005-6)
- Kellogg, J. N., & Vega, V. (1995). Tectonic development of Panama, Costa Rica, and the Colombian Andes: Constraints from global positioning system geodetic studies and gravity. *Special Paper of the Geological Society of America*, *295*(1), 75–90. <https://doi.org/10.1130/SPE295-p75>
- Li, W. X., Li, X. H., Wang, X. C., & Yang, D. S. (2017). Petrogenesis of Cretaceous shoshonitic rocks in the northern Wuyi Mountains, South China: A result of the roll-back of a flat-slab? *Lithos*, *288–289*, 125–142. <https://doi.org/10.1016/j.lithos.2017.06.014>
- Li, Z. X., & Li, X. H. (2007). Formation of the 1300-km-wide intracontinental orogen and postorogenic magmatic province in Mesozoic South China: A flat-slab subduction model. *Geology*, *35*(2), 179–182. <https://doi.org/10.1130/G23193A.1>
- Ligorria, J. P., & Ammon, C. J. (1999). Iterative deconvolution and receiver-function estimation. *Bulletin of the Seismological Society of America*, *89*(5), 1395–1400.
- Lloyd, G. E., Butler, R. W. H., Casey, M., & Mainprice, D. (2009). Mica, deformation fabrics and the seismic properties of the continental crust. *Earth and Planetary Science Letters*, *288*(1–2), 320–328. <https://doi.org/10.1016/j.epsl.2009.09.035>
- Ludwig, K. R. (2012). *Isoplot 3.75. A geochronological toolkit for Microsoft Excel, Special Publication* (Vol. 5). Berkeley: Berkeley Geochronology Center.
- Mantilla-Figueroa, L. C., Bissig, T., Valencia, V., & Hart, C. J. (2013). The magmatic history of the Vetás-California mining district, Santander massif, Eastern Cordillera, Colombia. *Journal of South American Earth Sciences*, *45*, 235–249. <https://doi.org/10.1016/j.jsames.2013.03.006>
- McDonough, W. F., & Sun, S. S. (1995). The composition of the Earth. *Chemical Geology*, *120*(3–4), 223–253. [https://doi.org/10.1016/0009-2541\(94\)00140-4](https://doi.org/10.1016/0009-2541(94)00140-4)
- Monsalve, M. L., Rojas, N. R., Velandia, F. A., Pintor, I., & Martínez, L. F. (2011). Caracterización geológica del cuerpo volcánico de Iza, Boyacá-Colombia. *Boletín de Geología*, *33*(1), 117–130.
- Montes, C., Hatcher, R. D. Jr., & Restrepo-Pace, P. (2005). Tectonic reconstruction of the northern Andean blocks: Oblique convergence and rotations derived from the kinematics of the Piedras-Girardot area, Colombia. *Tectonophysics*, *399*(1–4), 221–250. <https://doi.org/10.1016/j.tecto.2004.12.024>
- Mora, A., Ketcham, R. A., Higuera-Díaz, I. C., Bookhagen, B., Jimenez, L., & Rubiano, J. (2014). Formation of passive-roof duplexes in the Colombian Subandes and Perú. *Lithosphere*, *6*(6), 456–472. <https://doi.org/10.1130/L340.1>
- Mora, A., Parra, M., Forero, G., Blanco, V., Moreno, N., & Caballero, V. (2015). What drives orogenic asymmetry in the Northern Andes?: A case study from the apex of the Northern Andean Orocline. In C. Bartolini & P. Mann (Eds.), *Petroleum geology and potential of the Colombian Caribbean Margin, AAPG Memoir* (Vol. 108, pp. 547–586). <https://doi.org/10.1306/13531949M1083652>
- Mora, A., Parra, M., Strecker, M. R., Sobel, E. R., Hooghiemstra, H., Torres, V., & Vallejo-Jaramillo, J. (2008). Climatic forcing of asymmetric orogenic evolution in the Eastern Cordillera of Colombia. *Geological Society of America Bulletin*, *120*(7–8), 930–949. <https://doi.org/10.1130/B26186.1>
- Mora, A., Parra, M., Strecker, M. R., Sobel, E. R., Zeilinger, G., Jaramillo, C., et al. (2010). The eastern foothills of the Eastern Cordillera of Colombia: An example of multiple factors controlling structural styles and active tectonics. *Geological Society of America Bulletin*, *122*(11–12), 1846–1864. <https://doi.org/10.1130/B30033.1>
- Mora, A., Reyes-Harker, A., Rodríguez, G., Tesón, E., Ramírez-Arias, J. C., Parra, M., et al. (2013). Inversion tectonics under increasing rates of shortening and sedimentation: Cenozoic example from the Eastern Cordillera of Colombia. In M. Nemcok, A. Mora, & J. W. Cosgrove (Eds.), *Thick-skin dominated orogens: From initial inversion to full accretion*, Special Publications (Vol. 377, pp. 411–442). London: Geological Society. <https://doi.org/10.1144/SP377.6>
- Mora-Paez, H., Kellogg, J. N., Freymueller, J. T., Mencin, D., Fernandes, R. M. S., Diederix, H., et al. (2019). Crustal deformation in the northern Andes—A new GPS velocity field. *Journal of South American Earth Sciences*, *89*, 76–91. <https://doi.org/10.1016/j.jsames.2018.11.002>

- Mora-Paez, H., Mencin, D. J., Molnar, P., Diederix, H., Cardona-Piedrahita, L., Pelaez-Gaviria, J. R., & Corchuelo-Cuervo, Y. (2016). GPS velocities and the construction of the Eastern Cordillera of the Colombian Andes. *Geophysical Research Letters*, *43*, 8407–8416. <https://doi.org/10.1002/2016GL069795>
- Moyano, I., & Vallejo, E. (2015). Contribution to the knowledge of the Paipa geothermal system by the application of the magnetotelluric method. Proceedings World Geothermal Congress. Melbourne, Australia, 6pp.
- Nakamura, N. (1974). Determination of REE, Ba, Fe, Mg, Na, and K in carbonaceous and ordinary chondrites. *Geochimica et Cosmochimica Acta*, *38*(5), 757–775. [https://doi.org/10.1016/0016-7037\(74\)90149-5](https://doi.org/10.1016/0016-7037(74)90149-5)
- Pardo, N., Cepeda, H., & Jaramillo, J. M. (2005). The Paipa volcano, Eastern Cordillera of Colombia, South America: Volcanic stratigraphy. *Earth Sciences Research Journal*, *9*(1), 3–18.
- Pardo, N., Jaramillo, J. M., & Cepeda, H. (2005). The Paipa volcano, Eastern Cordillera of Colombia, South America (part II): Petrography and major elements petrology. *Earth Sciences Research Journal*, *9*(2), 148–164.
- Parra, M., Mora, A., Lopez, C., Rojas, L. E., & Horton, B. K. (2012). Detecting earliest shortening and deformation advance in thrust belt hinterlands: Example from the Colombian Andes. *Geology*, *40*(2), 175–178. <https://doi.org/10.1130/G32519.1>
- Parra, M., Mora, A., Sobel, E. R., Strecker, M. R., & González, R. (2009). Episodic orogenic front migration in the northern Andes: Constraints from low-temperature thermochronology in the Eastern Cordillera, Colombia. *Tectonics*, *28*, TC4004. <https://doi.org/10.1029/2008TC002423>
- Pearce, J. A. (1996). A user's guide to basalt discrimination diagrams. In D. A. Wyman (Ed.), *Trace element geochemistry of volcanic rocks: Applications for massive sulphide exploration*, Geological Association of Canada (Vol. 12, pp. 79–113). Short Course Notes.
- Peccerillo, A., Barberio, M. R., Yirgu, G., Ayalew, D., Barbieri, M., & Wu, T. W. (2003). Relationships between mafic and peralkaline silicic magmatism in continental rift settings: A petrological, geochemical and isotopic study of the Gedemsa volcano, central Ethiopian rift. *Journal of Petrology*, *44*(11), 2003–2032. <https://doi.org/10.1093/petrology/egg068>
- Pérez-Angel, L. C., & Molnar, P. (2017). Sea surface temperatures in the Eastern Equatorial Pacific and surface temperatures in the Eastern Cordillera of Colombia during El Niño: Implications for Pliocene conditions. *Paleoceanography*, *32*, 1309–1314. <https://doi.org/10.1002/2017PA003182>
- Porter, R., Zandt, G., & McQuarrie, N. (2011). Pervasive lower-crustal seismic anisotropy in Southern California: Evidence for underplated schists and active tectonics. *Lithosphere*, *3*(3), 201–220. <https://doi.org/10.1130/L126.1>
- Poveda, E., Monsalve, G., & Vargas, C. A. (2015). Receiver functions and crustal structure of the northwestern Andean region, Colombia. *Journal of Geophysical Research: Solid Earth*, *120*, 2408–2425. <https://doi.org/10.1002/2014JB011304>
- Renzoni, G. (1967). Geología del cuadrángulo J-12 Tunja. Ingeominas, informe 1546. 20pp.
- Restrepo, J. J., & Toussaint, J. F. (1988). Terranes and continental accretion in the Colombian Andes. *Episodes*, *11*, 189–193.
- Rodríguez, G., & Zapata, G. (2014). Descripción de una nueva unidad de lavas denominada Andesitas basálticas de El Morito - correlación regional con eventos magmáticos de arco. *Boletín de Geología*, *36*(1), 85–102.
- Rubatto, D. (2002). Zircon trace element geochemistry: Partitioning with garnet and the link between U–Pb ages and metamorphism. *Chemical Geology*, *184*(1–2), 123–138. [https://doi.org/10.1016/S0009-2541\(01\)00355-2](https://doi.org/10.1016/S0009-2541(01)00355-2)
- Saylor, J. E., Horton, B. K., Stockli, D. F., Mora, A., & Corredor, J. (2012). Structural and thermochronological evidence for Paleogene basement-involved shortening in the axial Eastern Cordillera, Colombia. *Journal of South American Earth Sciences*, *39*, 202–215. <https://doi.org/10.1016/j.jsames.2012.04.009>
- Schulte-Pelkum, V., & Mahan, K. H. (2014a). A method for mapping crustal deformation and anisotropy with receiver functions and first results from USArray. *Earth and Planetary Science Letters*, *402*, 221–233. <https://doi.org/10.1016/j.epsl.2014.01.050>
- Schulte-Pelkum, V., & Mahan, K. H. (2014b). Imaging faults and shear zones using receiver functions. *Pure and Applied Geophysics*, *171*(11), 2967–2991. <https://doi.org/10.1007/s00024-014-0853-4>
- Silva-Arias, A., Mantilla-Figueroa, L. C., & Terraza-Melo, R. (2010). Clasificación química y geotermometría de las cloritas de las formaciones cretácicas Santa Rosa y Lutitas de Macanal, cinturón esmeraldífero oriental, Cordillera Oriental de Colombia. *Boletín de Geología*, *32*(2), 45–54.
- Siravo, G., Faccenna, C., Gèrault, M., Becker, T. W., Fellin, M. G., Herman, F., & Molin, P. (2019). Slab flattening and the rise of the Eastern Cordillera, Colombia. *Earth and Planetary Science Letters*, *512*, 100–110. <https://doi.org/10.1016/j.epsl.2019.02.002>
- Siravo, G., Fellin, M. G., Faccenna, C., Bayona, G., Lucci, F., Molin, P., & Maden, C. (2018). Constraints on the Cenozoic deformation of the Northern Eastern Cordillera, Colombia. *Tectonics*, *37*, 4311–4337. <https://doi.org/10.1029/2018TC005162>
- Sláma, J., Košler, J., Condon, D. J., Crowley, J. L., Gerdes, A., Hanchar, J. M., et al. (2008). Plešovice zircon—A new natural reference material for U–Pb and Hf isotopic microanalysis. *Chemical Geology*, *249*(1–2), 1–35. <https://doi.org/10.1016/j.chemgeo.2007.11.005>
- Syracuse, E. M., Maceira, M., Prieto, G. A., Zhang, H., & Ammon, C. J. (2016). Multiple plates subducting beneath Colombia, as illuminated by seismicity and velocity from the joint inversion of seismic and gravity data. *Earth and Planetary Science Letters*, *444*, 139–149. <https://doi.org/10.1016/j.epsl.2016.03.050>
- Taboada, A., Rivera, L. A., Fuenzalida, A., Cisternas, A., Philip, H., Bijwaard, H., et al. (2000). Geodynamics of the northern Andes: Subductions and intracontinental deformation (Colombia). *Tectonics*, *19*(5), 787–813. <https://doi.org/10.1029/2000TC900004>
- Tatham, D. J., Lloyd, G. E., Butler, R. W. H., & Casey, M. (2008). Amphibole and lower crustal seismic properties. *Earth and Planetary Science Letters*, *267*(1–2), 118–128. <https://doi.org/10.1016/j.epsl.2007.11.042>
- Tesón, E., Mora, A., Silva, A., Namson, J., Teixell, A., Castellanos, J., et al. (2013). Relationship of Mesozoic graben development, stress, shortening magnitude, and structural style in the Eastern Cordillera of the Colombian Andes. In M. Nemck, A. Mora, & J. W. Cosgrove (Eds.), *Thick-skin dominated orogens: From initial inversion to full accretion*, Special Publications (Vol. 377, pp. 257–283). London: Geological Society. <https://doi.org/10.1144/SP377.10>
- Thybo, H., & Artemieva, I. M. (2013). Moho and magmatic underplating in continental lithosphere. *Tectonophysics*, *609*, 605–619. <https://doi.org/10.1016/j.tecto.2013.05.032>
- Tiepolo, M., & Tribuzio, R. (2008). Petrology and U–Pb zircon geochronology of amphibole-rich cumulates with sanukitic affinity from Husky Ridge (Northern Victoria Land, Antarctica): Insights into the role of amphibole in the petrogenesis of subduction-related magmas. *Journal of Petrology*, *49*(5), 937–970. <https://doi.org/10.1093/petrology/egn012>
- Trenkamp, R., Kellogg, J., Freymueller, J., & Mora, H. (2002). Wide plate margin deformation, southern Central America and northwestern South America, CASA GPS observations. *Journal of South American Earth Sciences*, *15*(2), 157–171. [https://doi.org/10.1016/S0895-9811\(02\)00018-4](https://doi.org/10.1016/S0895-9811(02)00018-4)
- Van der Lelij, R., Spikings, R., & Mora, A. (2016). Thermochronology and tectonics of the Merida Andes and the Santander Massif, NW South America. *Lithos*, *248–251*, 220–239. <https://doi.org/10.1016/j.lithos.2016.01.006>

- Vargas, C. A., & Mann, P. (2013). Tearing and breaking off of subducted slabs as the result of collision of the Panama Arc-indentor with northwestern South America. *Bulletin of the Seismological Society of America*, 103(3), 2025–2046. <https://doi.org/10.1785/0120120328>
- Vásquez, M., & Altenberger, U. (2005). Mid-Cretaceous extension-related magmatism in the eastern Colombian Andes. *Journal of South American Earth Sciences*, 20(3), 193–210. <https://doi.org/10.1016/j.jsames.2005.05.010>
- Vásquez, M., Altenberger, U., Romer, R. L., Sudo, M., & Moreno-Murillo, J. M. (2010). Magmatic evolution of the Andean Eastern Cordillera of Colombia during the Cretaceous: Influence of previous tectonic processes. *Journal of South American Earth Sciences*, 29(2), 171–186. <https://doi.org/10.1016/j.jsames.2009.02.003>
- Vervoort, J. D., & Blichert-Toft, J. (1999). Evolution of the depleted mantle: Hf isotope evidence from juvenile rocks through time. *Geochimica et Cosmochimica Acta*, 63(3-4), 533–556. [https://doi.org/10.1016/S0016-7037\(98\)00274-9](https://doi.org/10.1016/S0016-7037(98)00274-9)
- Vervoort, J. D., & Patchett, P. J. (1996). Behavior of hafnium and neodymium isotopes in the crust: Constraints from Precambrian crustally derived granites. *Geochimica et Cosmochimica Acta*, 60(19), 3717–3733. [https://doi.org/10.1016/0016-7037\(96\)00201-3](https://doi.org/10.1016/0016-7037(96)00201-3)
- Vervoort, J. D., Patchett, P. J., Soderlund, U., & Baker, M. (2004). Isotopic composition of Yb and the determination of Lu concentrations and Lu/Hf ratios by isotope dilution using MC-ICPMS. *Geochemistry, Geophysics, Geosystems*, 5, Q11002. <https://doi.org/10.1029/2004GC000721>
- Vesga, A. M., & Jaramillo, J. M. (2009). Geoquímica del domo volcánico en el municipio de Iza, departamento de Boyacá; interpretación geodinámica y comparación con el vulcanismo neógeno de la cordillera oriental. *Boletín de Geología*, 31(2), 97–108.
- Wagner, L. S., Jaramillo, J. S., Ramírez-Hoyos, L. F., Monsalve, G., Cardona, A., & Becker, T. W. (2017). Transient slab flattening beneath Colombia. *Geophysical Research Letters*, 44, 6616–6623. <https://doi.org/10.1002/2017GL073981>
- Wiedenbeck, M., Allé, P., Corfu, F., Griffin, W. L., Meier, M., Oberli, F., et al. (1995). Three natural zircon standards for U-Th-Pb, Lu-Hf, trace element and REE analyses. *Geostandards and Geoanalytical Research*, 19(1), 1–23. <https://doi.org/10.1111/j.1751-908X.1995.tb00147.x>
- Williams, I. S. (1998). U-Th-Pb geochronology by ion microprobe. In M. A. McKibben, W. C. Shanks, III, & W. I. Ridley (Eds.), *Applications of microanalytical techniques to understanding mineralizing processes*, *Reviews in Economic Geology* (Vol. 7, pp. 1–35).
- Winchester, J. A., & Floyd, P. A. (1977). Geochemical discrimination of different magma series and their differentiation products using immobile elements. *Chemical Geology*, 20, 325–343. [https://doi.org/10.1016/0009-2541\(77\)90057-2](https://doi.org/10.1016/0009-2541(77)90057-2)
- Woodhead, J. D., & Hergt, J. M. (2005). A preliminary appraisal of seven natural zircon reference materials for in situ Hf isotope determination. *Geostandards and Geoanalytical Research*, 29(2), 183–195. <https://doi.org/10.1111/j.1751-908X.2005.tb00891.x>